

MODELING OF CATALYTIC COUPLING OF METHANE

Lucy M. Hair, William J. Pitz, Michael W. Droege and Charles K. Westbrook
Lawrence Livermore National Laboratory
P.O. Box 808 Livermore, CA 94551

Keywords: oxidative coupling of methane, chemical kinetic model, catalysis modeling

Catalytic oxidative coupling to ethane or ethylene is an appealing, direct route to utilization of otherwise low value natural gas located in remote sites. Researchers have focused on oxidative coupling of methane for about 15 years, using metal oxide catalysts to facilitate the reaction (1-6). Despite intensive efforts, the best yields to C₂ hydrocarbons have been in the 20 to 30 % range, generally accomplished with catalysts which include an alkali metal on an alkali earth oxide, e.g., Li/MgO (6b).

In an attempt to understand and overcome the source of this limitation, more fundamental catalyst studies and modeling have been undertaken. Labinger and Ott (7) measured kinetic rate constants and modeled the catalytic process for ARCO's oxidative coupling catalyst, achieving good agreement with reactor data. Labinger in a further analysis (8) based on their model found that the C₂ yield is limited to 30% by sequential oxidation of ethylene as methane conversion increases. Kimble and Kolts were also able to model the catalytic-homogeneous process for their system (9).

The importance of the thermally-induced, homogeneous, gas-phase reactions cannot be neglected in any such model. Much of the recent work in oxidative coupling has explicitly recognized the fact that under most conditions, thermally-induced reactions account for a large fraction of products (10-14). In previous work (15-16), we employed a chemical kinetic model (HCT), developed at this Laboratory, to describe the overall homogeneous gas phase reactions of methane and oxygen. The HCT model can be used to describe reaction pathways and determine products for a wide variety of reactor types and conditions. Its application successfully predicted methane conversions and product distributions found experimentally for a reactor containing no catalyst. In this work, we expand the HCT model to include proposed catalytic reaction schemes. Our purpose is to predict limits in C₂ yield, describe product trends as a function of generalized catalyst behavior and use these results as a guide to catalyst design.

Gas-Phase Model

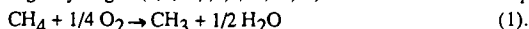
The gas-phase chemical kinetic model used in the present study is the HCT (Hydrodynamics, Chemical kinetics and Transport) model (17). This model solves the coupled equations of conservation of mass, momentum and energy in finite difference form, and determines each chemical species concentration. For this study, the reactor is assumed to be essentially a plug flow system where spatial variations in velocity, temperature and species concentrations in the radial direction and diffusion of energy and species in the axial direction are assumed to be negligible. Spatial changes in species concentration and temperature can therefore be replaced by time variations. Thus only the energy equation and the species conservation equations must be solved. Surface reactions at the reactor wall were not considered. In the numerical model, coupling between the different chemical species takes place through the chemical kinetic terms, and these terms are introduced into the model through a detailed reaction mechanism.

The chemical reaction mechanism used here has developed from a number of studies of methane

and natural gas combustion. This mechanism has been extensively validated in a series of studies where numerical results were compared to experimental results from static reactors, stirred reactors, shock tubes, flames and flow reactors (18-22).

Inclusion of Catalytic Methane Activation

A schematic of the mechanistic pathways leading to the gas-phase oxidation of methane by oxygen is shown in Fig. 1. We have added reactions to the chemical kinetic mechanism to treat the effect of introducing a catalyst. It is generally assumed that the effectiveness of oxidative coupling catalysts stems from their ability to activate methane. Thus, the first step was to determine the effect of methane activation alone. Considerable experimental evidence suggests that the catalyst activates methane by abstracting a hydrogen (2,4,6a,i,7,9,11,23,24). We have modeled this process as the global step,



We assumed the reaction rate is given by the expression,

$$R_1 = k_1 [\text{CH}_4][\text{O}_2]^a \quad (2).$$

The dependence of the rate on $[\text{O}_2]^a$ serves to turn off the catalytic reaction when the gas phase oxygen is depleted. An exponent "a" of 1.0 serves this purpose satisfactorily, since we do not know the series of elementary reactions. Computationally, it appears that the overall reaction is not critically dependent on the value of the "a" exponent.

A series of calculations were performed with the above "catalytic" reaction added to the gas-phase chemical kinetic mechanism in order to explore the effect of catalyst activity (k_1) on predicted C_2 yield. The conditions considered were a 2:1 molar ratio of $\text{CH}_4:\text{O}_2$ in a 75% Ar mixture. The reactor temperature and pressure were maintained at a constant 750 C and 1 atm, resp. The curve in Fig. 2 shows the results of these calculations, where the residence time for the upper curve was optimized for maximum yield and the residence time for the lower curve was 10 s. The methane conversion and product distributions are shown in Table 1. It is predicted that for k_1 equal to $10^7 \text{ M}^{-1}\text{s}^{-1}$, the maximum C_2 yield is 84%. When no catalyst is present, the gas-phase reactions result in a C_2 yield of about 0.4% under these conditions of high dilution. The calculations indicate that the catalyst does not substantially affect the yield until the catalytic methane activation rate constant reaches about 10^1 . The C_2 yield reaches about 70% for a methane activation rate constant of 10^7 . This yield would certainly be adequate to justify production; obviously, either catalysts do not achieve such a high rate constant or they perform another function, such as oxidation.

Although the gas-phase reactions in the absence of catalyst yield only 0.4% C_2 's, once the catalyst has generated the methyl radical, it is available for any further reactions. At a sufficiently high level of catalyst activity, the high concentration of methyl radicals will drive the coupling reaction in preference to oxidation steps. Then at short residence times, the catalytic methane activation and gas-phase coupling steps will be sufficient to predict products. Thus it is of interest to know the relative contribution of gas-phase vs catalytic reactions to the overall conversion of methane. To determine these relative contributions, we integrated over time the rates of methane conversion due to the catalyst and to gas-phase reactions for values of k_1 of 10^3 , 10^4 and 10^5 . These results are shown in Fig. 3. As expected, the catalyst contributes virtually all of the methane conversion at early times until a sufficient radical pool is established for gas-phase reactions. A steady state conversion is reached by about 7 s, 0.3 s and 0.06 s for k_1 of 10^3 , 10^4 and 10^5 , resp. At steady state, 20%, 50% and 70% of the methane is converted due to catalytic action for values of k_1 equal to 10^3 , 10^4 and 10^5 , resp. The

catalyst dominates methane conversion for values of the methane activation rate constant greater than 10^4 .

Now we investigate the effect of moving away from our optimized residence time. The methane conversion and product distributions corresponding to the predicted maximum C_2 yields for values of k_1 of 10^2 to 10^5 are shown in Table 1. The methane conversion increases from 23.3 to 53.7%, while the selectivity to C_2 's increases from 44.5 to 67.1%. The major increase in C_2 's is due to an increase in ethane from 18.7 to 41.6%. The residence times which result in maximum C_2 yields decrease from 3.4 to 0.03 s as k_1 increases from 10^2 to 10^5 . Since the gas-phase coupling reaction to form ethane is rapid relative to dehydrogenation to ethylene, at shorter residence times, one would expect a higher ethane/ethylene split. The calculated methane conversion and product distributions at 10s residence time, displayed in Table 2, show that this is indeed true. At longer residence times, the C_2 yield decreases slowly, the methane conversion increases, and the C_2 selectivity decreases along with selectivity to ethane. Regardless of residence time, carbon monoxide accounts for the majority of COX products.

Comparison of Model Predictions with Experimental Data

Values of k_1 and the corresponding C_2 yield for catalysts known to be effective in oxidative coupling of methane (6b-h) and run under similar conditions to those run for the model are also shown in Fig. 2. In calculating k_1 from literature data, it was assumed that the rate of methyl radical production was equal to the rate of methane conversion and was, therefore, determined from the experimental methane feed rate and the final methane conversion. The rate constant k_1 was then found by dividing that rate by the methane and oxygen concentrations in the feed at reaction temperature. As shown in Fig. 2, the fit of model predictions to rate constants calculated from experimental results is quite good. The values of k_1 that we determined range from 10^2 to 10^5 , corresponding to measured C_2 yields of 3-20%, while the model predicts C_2 yields increasing from 8-35%. The methane activation rate constants for these coupling catalysts are too low to achieve the high C_2 yields possible from our model calculations. Even the more active catalysts do not give C_2 yields of 35%, as the model predicts. In fact, for methane activation rate constants of 10^3 and greater, the experimental C_2 yield is fairly flat as a function of catalyst activity. Table 3 shows a selection of data for coupling catalysts (6b-d). The fit of the model to C_2 yield, methane conversion and selectivity to C_2 's is quite reasonable, matching best at model residence times slightly greater than those optimized for C_2 yield. In a few cases, the predicted ethane/ethylene split is very close to literature values, and fairly good for the others.

The model does not predict carbon dioxide as the only oxidation product, as is seen in the data. It seems likely that the carbon dioxide is produced directly by a catalytic route, bypassing the gas-phase reactions that would lead from ethylene to carbon monoxide. Such a catalytic process could also explain the cap on C_2 yield observed for the coupling catalysts.

Summary

Overall, this simple modification of the gas-phase kinetic model to include a global catalytic step that only produces methyl radicals agrees reasonably well with experimental data. The model predicts that a methane activation catalyst with a sufficiently high rate constant, which performed no other function, could result in a C_2 yield of at least 70%. The high methane activation rate constant is needed

to overcome gas-phase oxidation reactions. The highest methane activation rate constant determined from experimental data was on the order of $10^5 \text{ M}^{-1}\text{s}^{-1}$, corresponding to a predicted C_2 yield of 35%, but actually yielding only about 20%. A catalytic reaction leading from ethylene to carbon dioxide could account both for the lowered yield and for the absence of carbon monoxide in experimental work.

References

1. Pitchai, R.; Klier, K. *Catal.Rev.Sci.Eng.* **1986**, 28, 13.
2. Lee, J.S.; Oyama, S.T. *Catal.Rev.Sci.Eng.* **1988**, 30, 249.
3. Hutchings, G.J.; Scurrell, M.S.; Woodhouse, J.R. *Chem.Soc.Rev.* **1989**, 18, 251.
4. Lunsford, J.H. *Catal.Today* **1990**, 6(3), 235.
5. Garibyan, T.A.; Margolis, L.Y. *Catal.Rev.Sci.Eng.* **1989-1990**, 31, 355.
6. a). Keller, G.E.; Bhasin, M.M. *J.Catal.* **1982**, 73, 9.
 b). Ito, T.; Lunsford, J.H. *Nature* **1985**, 314, 721.
 c). Otsuka, K.; Liu, Q.; Morikawa, A., *Inorg.Chim.Acta* **1986**, 118, L23.
 d). Machida, K.I.; Enyo, M. *J.Chem.Soc., Chem.Comm.* **1987**, 1639.
 e). France, J.E.; Shamsi, A.; Ahsan, M.Q. *Energy & Fuels* **1988**, 2, 235.
 f). Matsuura, I.; Utsumi, Y.; Nakai, M. *Chem.Lett.* **1986**, 1981.
 g). Otsuka, K.; Komatsu, T. *J.Chem.Soc., Chem.Comm.* **1987**, 388..
 h). Aika, K.; Moriyama, T.; Takasaki, N. Iwamatsu, E. *J.Chem.Soc., Chem.Comm.* **1986**, 1210.
 i). Sofranko, J.A.; Leonard, J.J.; Jones, C.A. *J.Catal.* **1987**, 103, 302.
 j). Thomas, J.M.; Kuan, X.; Stachurski, J. *J.Chem.Soc., Chem.Comm.* **1988**, 162.
 k). Korf, S.J.; Roos, J.A.; Derksen, J.W.H.C.; Vreeman, J.A.; Van Ommen, J.G.; Ross, J.R.H. *Appl.Catal.* **1990**, 59, 291.
 l). Ahmed, S.; Moffat, J.B. *J.Catal.* **1990**, 125, 54.
 m). Agarwal, S.K.; Migone, R.A.; Marcelin, G. *J.Catal.* **1990**, 121, 110.
 n). Choudhary, V.R.; Chaudhari, S.T.; Rajput, A.M.; Rane, V.H. *J.Chem.Soc., Chem.Comm.* **1989**, 1526.
7. Labinger, J.A.; Ott, K.C. *J.Phys.Chem.* **1987**, 91, 2682.
8. Labinger, J.A., *Cat.Lett.* **1988**, 1, 371.
9. Kimble, J.B.; Kolts, J.H. *Energy Prog.* **1986**, 6 (4), 226.
10. Lane, G.S.; Wolf, E.E. *J.Catal.* **1988**, 113, 144.
11. Zanthoff, H.; Baerns, M. *Ind.Eng.Chem.Res.* **1990**, 29, 2.
12. Yates, D.J.C.; Zlotin, N.E. *J.Catal.* **1988**, 111, 317.
13. Nelson, P.F.; Cant, N.W. *J.Phys.Chem.* **1990**, 94, 3756.
14. Ekstrom, A.; Lapszewicz, J.A.; Campbell, I. *Appl.Catal.* **1989**, 56, L29.
15. Drooge, M.W.; Hair, L.M.; Pitz, W.J.; Westbrook, C.K. Lawrence Livermore National Laboratory Report UCRL-100568 **1989**.
16. Drooge, M.W.; Hair, L.M.; Pitz, W.J.; Westbrook, C.K. in *Proc. 1989 SPE Gas Tech. Symp.* **1989**, Dallas, TX., p. 247.
17. Lund, C.M. University of California Lawrence Livermore National Laboratory Report UCRL-52504. **1978** Revised by Lila Chase, 1989.

18. Westbrook, C.K.; Pitz, W.J. *Combust.Sci.Technol.* **1984**, 37, 117.
19. Westbrook, C.K.; Creighton, J.; Lund, C.; Dryer, F. *J.Phys.Chem.* **1977**, 81, 2542.
20. Westbrook, C.K. *Combust.Sci.Technol.* **1979**, 20, 5.
21. Wilk, R.D.; Cernansky, N.P.; Pitz, W.J.; Westbrook, C.K. *Combustion Flame* **1989**, 77, 145
22. Pitz, W.J.; Westbrook, C.K.; Proscia, W.M.; Dryer, F.L. **Twentieth Symposium (International) on Combustion**, The Combustion Institute: Pittsburgh, 1985, p.831.
23. Driscoll, D.J.; Martin, W.; Wang, J.-X.; Lunsford, J.H. *J.Am.Chem.Soc.* **1985**, 107, 58.
24. Mims, C.A.; Hall, R.B.; Rose, K.D.; Myers, G.R. *Catal.Lett.* **1989**, 2, 361.

Table 1
Predictions of Model at Maximum C2 Yield

kl (M ⁻¹ s ⁻¹)	Max	%CH4	%C2	%C2H4	%C2H6	%CO	%CO2
	%C2	Conv					
	Yld						
10 ²	10.4	23.3	44.5	25.8	18.7	51.5	3.1
10 ³	15.8	25.0	63.2	32.2	31.0	34.8	0.9
10 ⁴	24.7	35.1	70.2	33.4	36.8	28.2	0.5
10 ⁵	35.1	52.3	67.1	25.5	41.6	14.6	0.1

Table 2
Predictions of Model at 10s Residence Time

kl (M ⁻¹ s ⁻¹)	%C2	%CH4	%C2	%C2H4	%C2H6	%CO	%CO2
	Yld	Conv					
10 ²	7.5	46.4	16.1	13.2	2.9	71.9	11.6
10 ³	11.0	51.3	21.5	19.0	2.5	71.0	6.9
10 ⁴	17.9	57.3	31.3	27.5	3.8	64.6	3.1
10 ⁵	30.6	67.5	45.5	39.4	6.1	52.1	1.1

Table 3
Experimental Results from Literature

Ref	%C2 Yield	%CH4 Conv	%C2	%C2H4	%C2H6	%CO	%CO2
6b	19.0	37.8	50.5	31.0	19.5	0.0	49.6
	19.4	42.8	45.5	29.0	16.5	0.8	53.7
6c ⁱ	18.6	25.9	71.8	56.2	15.6	—	—
6c ⁱⁱ	13.2	25.8	51.3	23.4	27.9	—	—
6d	31.8	45.1	60.1	36.1	24.0	0.0	39.9

6b. 7%Li/MgO, 4g: 720 C, 2:1 CH₄:O₂, 89% He Diln.

6c. (i) 20 mol% LiCl/NiO (ii) 20 mol% LiOH/NiO: 750 C, CH₄:O₂ 2:1, 94% He diln., 1 g cat.

6d. SrCeYbO, 0.6 g: 750 C, CH₄:O₂ 2:1, 80% diln with He.

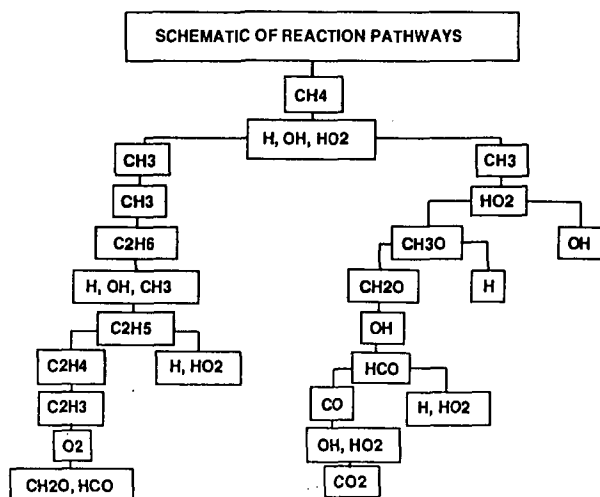


Figure 1. Schematic of gas-phase mechanism for methane oxidation.

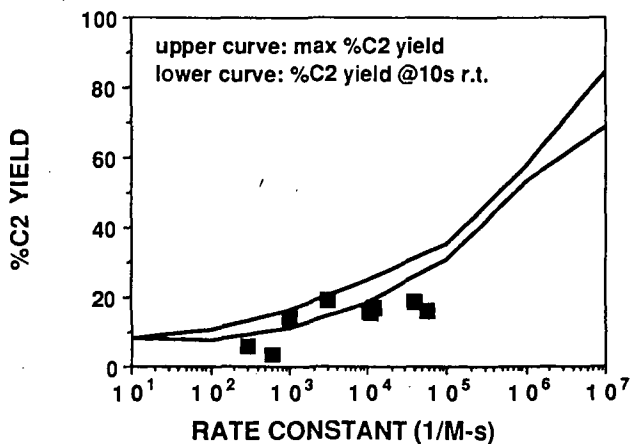


Figure 2. Predicted and experimental C₂ yields as a function of catalytic methane activation rate constant, k_1 . Conditions: 750 C, 2:1 CH₄:O₂, 75% Ar dilution.

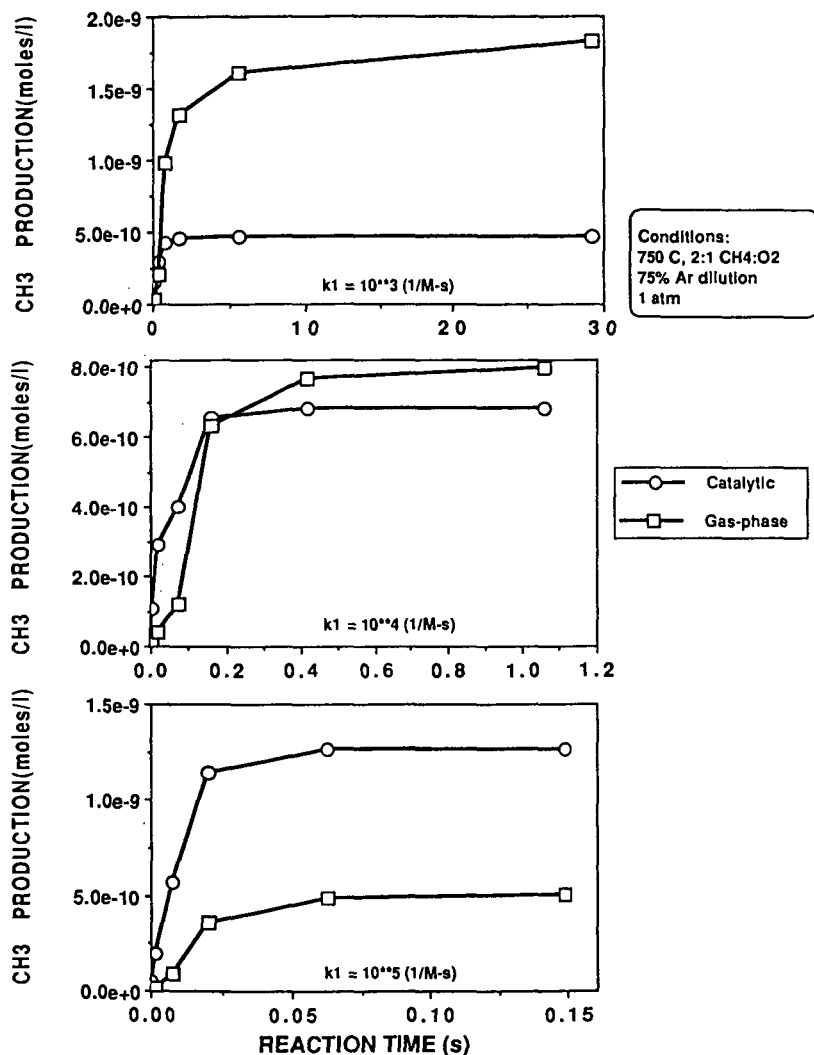


Figure 3. Comparison of methyl production due to catalytic and gas-phase reactions. a) $k_1=10^3$. b) $k_1=10^4$. c) $k_1=10^5$. Units= $M^{-1}s^{-1}$.

SYMPOSIUM ON COMPUTER APPLICATIONS IN FUEL CHEMISTRY
PRESENTED BEFORE THE DIVISION OF FUEL CHEMISTRY
AMERICAN CHEMICAL SOCIETY
ACS INTERNATIONAL MEETING, ATLANTA, GA
APRIL 14-19, 1991

AN ASSESSMENT OF THE PREDICTIVE CAPABILITIES OF
A COMPUTATIONAL MODEL FOR FUEL THERMAL STABILITY

Jeffrey A. Pearce, K. V. Reddy, and W. M. Roquemore
Aero Propulsion and Power Directorate
Wright Laboratory
Wright-Patterson AFB, OH 45433

Keywords: Fuel Thermal Stability, Modeling, Computational Fluid Dynamics

INTRODUCTION

The thermal stability of jet fuels is one of the major impediments facing the aerospace community in attempting to increase aircraft performance. Fuel is widely used as a coolant for critical on-board systems, and the thermal loads on the fuel resulting from this practice are steadily increasing. If this trend continues, the thermal stability limit of the fuel will soon be reached and the cooling capacity of current fuels would be exhausted. Restrictions on design parameters, particularly the maximum allowable fuel temperature, will soon be a key limiting factor in attempts to improve overall performance. Ideally, one desires a fuel which remains stable at extreme temperatures ($> 1000^{\circ}\text{F}$), but realistically any tangible improvement in fuel stability would be welcomed. However, after decades of study, little is known of the fundamental processes leading to the deposition of solid materials on fuel system components largely due to the complexity of the processes involved, which include fuel degradation chemistry, heat transfer, and fluid mechanics.

Recent research has focused on the possibility of modeling fuel thermal stability using Computational Fluid Dynamics (CFD) with a global chemistry model. This approach allows one to examine different hypotheses about deposition mechanisms with relative speed and great flexibility. An essential element in the development of these models regards the formulation of the degradation chemistry. Typical fuels are extremely complex mixtures of hydrocarbons; therefore, attempting to model the specific reactions which contribute to deposition would be a nearly impossible chore. However, global representations of the degradation chemistry are a simple and often effective alternative to applying the full detailed chemistry.

To date, modeling efforts have focused on simulating heated tube experiments using simple, global autooxidation chemistry models^{1,2}. These models have performed adequately in predicting the results of other heated tube experiments; however, their ability to predict the results of experiments with significantly different boundary conditions is questionable. Such an experiment has recently been performed at Purdue University³ in an effort to examine the relative effects of wall and bulk fuel temperature on the deposition process. This experiment features conditions which vary greatly from those encountered in typical heated tube experiments; consequently, this experiment offers a unique vehicle with which to test and improve the current formulation of the models.

The purpose of this paper is to examine the predictive capabilities of a particular thermal stability model. This examination includes addressing the model's ability to predict the results of two basic classes of experiments: (1) constant heat flux heated tube experiments, similar to the experiments from which the model was devised and (2) constant wall temperature experiments. The results of these predictions yield valuable insights into the model's capabilities and indicate areas for possible improvement.

THERMAL STABILITY MODEL

Argonne National Laboratory/Air Force (ANL/AF) Model

The particular model applied in this study was developed by the Argonne National Laboratory in conjunction with the Air Force^{1,2}. The intent of this model is to provide the capability to predict

deposition within a given fuel system component. Ultimately, related models will be employed to minimize the ill effects of fuel degradation on various fuel system components. However, it is important to note that the model is in a developmental stage and is not yet suitable for general, widespread use as a design tool.

The approach to predicting deposition with the model is based on a two-dimensional computational fluid dynamics (CFD) code. This approach offers great generality in that given the wall condition (temperature/heat flux), tube geometry, and inlet conditions (velocity and temperature) the code can predict the overall solution of the flow field including the wall and bulk fuel temperatures, pressure, radial and axial velocity components, and constituent concentrations (O_2 , precursor, deposit) throughout the domain. By applying the CFD approach, the inherent coupling which exists between the chemistry, heat transfer, and fluid mechanics is preserved.

The essence of modeling fuel thermal stability lies in the degradation chemistry, which for this model is subdivided into two portions: (1) reactions occurring in the bulk fuel and (2) reactions occurring at the wall. In the bulk fuel, the following reactions apply:



where Equation 1 represents the formation of deposit precursors in the bulk fuel and Equation 2 represents the destruction of precursors at high temperatures. It is assumed that any precursor reaching the solid surface by means of diffusive and convective transport immediately forms a solid deposit on the wall. The remainder of the chemistry is a reaction at the wall whereby deposits are formed directly in the following manner:



The specific reaction rates for Equations 1-3 are based on Arrhenius expressions such as Equation 4 below:

$$k_n = A_n \exp(-E_n/RT) \quad (4)$$

Note that Equations 1 and 2 are based on the local *fuel* temperature while Equation 3 is based on the *wall* temperature.

After exercising the code, it becomes apparent that the deposition from the wall autooxidation reaction, represented by Equation 3, is only a small fraction of the overall deposition predicted with this model for cases where the temperature exceeds 475 K. Nonetheless, the low activation energy used for the wall autooxidation reaction ($E_3 = 8$ kcal/mole) provides a small amount of deposit on the tube walls when the wall temperature is close to room temperature. Since the bulk reactions tend to dominate the deposition process at higher temperatures, it is the bulk fuel temperature along with the dissolved oxygen concentration that are the primary drivers of fuel degradation in this code. Regarding the formation of deposits on the solid wall, which is the eventual product of the calculation, there are two mechanisms by which this occurs: (1) precursors formed in the bulk fuel (Equation 1) can reach the wall by diffusive and convective transport to form deposits and (2) deposits can be formed directly on the wall by Equation 3.

The values of the constants for the activation energies (E_n) and pre-exponential factors (A_n) were determined from experimental data^{4,5,6}. These experiments, described below, consisted of flowing JP-5 over an electrically heated tube (constant heat flux) and measuring the deposition accumulated on the tube surface. The oxygen concentration at the tube inlet was taken to be the saturation value of approximately 55 ppm by weight. Values for A_n and E_n can be found in Table 1.

EXPERIMENTS MODELED

Three different experimental test cases were examined using the model described above. Two of these experiments are constant heat flux heated tube experiments which have obvious similarities. The third experiment, however, offers a challenge to the model in that the boundary conditions are quite

different than the heated tube experiments used to calibrate the model. This third experiment is a device developed at Purdue University³ to examine the relative effects of wall and bulk fuel temperature on the observed deposition.

Heated Tube Experiments

The heated tube experiment is a widely used tool in the study of fuel thermal stability. In these experiments, fuel (initially at ambient temperature) is passed through a cylindrical metal tube which is heated by electrical resistance to thermally stress the fuel. Deposits accumulate on the tube as a result of the thermal stressing, and the deposit mass is measured to determine the degree of degradation. Some characteristics of this test are that a constant heat flux is applied to the fuel as a result of the electrical resistance heating method, and both the bulk fuel and wall temperatures increase at a roughly linear rate over the length of the tube. Data from two sets of heated tube experiments were used for model evaluations in this effort: (1) data from Marteney and Spadaccini^{4,5,6} which was used to calibrate the chemical constants in the ANL/AF model, and (2) data from Giovanetti and Szelc^{7,8} from similar heated tube experiments using Jet-A fuel. For both data sets the fuel was air sparged and no fuel was recirculated.

Purdue Copper Block Test

Juxtaposed against the heated tube experiments which are typical in thermal stability research, the Copper Block Test developed at Purdue³ is markedly different. Many differences between this experiment and the heated tube experiments are clearly apparent. Chief among these differences is the manner in which the two experiments endeavor to stress the fuel. In the heated tube experiments, a constant heat flux is applied to the fuel which results in linearly increasing profiles of fuel and wall temperature along the length of the tube. The Purdue test features JP-8 flowing through a cylindrical metal tube which is embedded between two heated copper blocks. The high thermal conductivity of the copper results in a nearly constant tube wall temperature which implies a decreasing heat flux with length as bulk temperature increases. Additional features of the experiment include preheating of the fuel to temperatures (> 500 K) which are in the regime of significant fuel degradation. However, there are other subtle differences that can have a profound effect on the experimental results.

The Purdue test lacks much of the oxygen available in the heated tube experiments as the fuel is recirculated (approximately 4-5 passes through the tube in a 6 hour test) and is not air/oxygen sparged. In fact, further reduction in the fuel's oxygen content results from the practice of maintaining a N_2 overpressure on the fuel in the accumulator. Nonetheless, perhaps the most significant difference between the two experiments is the magnitude of the temperatures in the experiments. In general, the maximum temperature in the heated tube experiments is in the vicinity of 650 K, where the Purdue test reaches temperatures of 750 K. This difference in the maximum temperature could possibly account for a change in the deposition mechanism from oxidative to pyrolytic. In all, it would appear that this test bears little resemblance to the test employed to calibrate the model.

This claim is substantiated by the findings of the researchers at Purdue. In examining deposition data from their experiment against the data of Tevelde and Glickstein⁹ (from another constant heat flux heated tube experiment) they found that there was a large discrepancy between the results. Figure 1 shows this discrepancy where the Purdue data appear to show the deposition rate increasing steadily with wall temperature while the Tevelde and Glickstein data clearly show the deposition rate peaking at ~ 650 K and decreasing at higher temperatures. It is our belief that a properly devised model should be able to predict both data sets accurately, and that the differences observed are merely due to the differences in the experimental methodology. Fortunately, these observed differences offer the opportunity to examine some capabilities and shortcomings of the current model formulation.

RESULTS

Predictions of Heated Tube Data

The initial task in terms of exercising the model was to calibrate the chemical constants (A_n and E_n). This was done by modeling the heated tube experiments of Marteney and Spadaccini^{4,5,6} carefully tuning the chemical reaction constants (Table 1). In the calibration experiments, JP-5 fuel is driven through a long, thin long metal tube (0.237 cm ID \times 2.4 m length) at a velocity of 2.1 m/s while the tube is being heated with a constant electrical power source. The high inlet fuel velocity makes the entire

flow in the tube turbulent; therefore, turbulent flow simulations have been used to predict the deposition rates under these flow conditions. Figure 2 demonstrates that the calibrated ANL/AF model does an extremely good job of representing the experimental data. In particular, the agreement between the model and the data are extremely good in the region between 500-600 K. Note the change in the slope of the curve at ~ 500 K representing the point at which the reaction in the bulk fuel begins to dominate the wall reaction. As a whole, the model is quite capable of accurately representing the data from which it was calibrated.

Figure 3 shows the model's prediction of the experiments of Giovanetti and Szetela^{7,8}. One can clearly see that the model predicts the experimental data with reasonable accuracy. There is a wide scatter in the data (greater than an order of magnitude) in the region below 500 K, so it is difficult to say whether the model is representative of the data in this temperature range. However, in the region between 500-560 K, the model yields very good results and follows the sharp rise in the deposition rate. Other key features of the deposition curve are also accurately predicted; in particular, the value of the maximum deposition rate and the temperature at which it occurs are both well represented. Furthermore, the sharp decrease in the deposition rate following the peak value is also well represented by the model. The general accuracy of the model in predicting these data is encouraging, since these are not the experiments used to calibrate the model. Nonetheless, one must consider the basic similarities between the experiments modeled in Figure 3 and the experiments used to calibrate the model. All are constant heat flux heated tube experiments utilizing similar fuels (JP-5 and Jet-A) in nearly identical geometries. Quantities such as the heat flux and the mass flow rate do differ, but the experiments are exceedingly similar. Consequently, the high quality of the model predictions for these cases does not guarantee the model's predictive capabilities.

Predictions of Purdue Data

The initial calculations performed to model the Purdue experiment were done with the model in its calibrated form, and the results are provided in Figure 4. For reference, these calculations were carried out for an inlet fuel temperature of 523 K with the constant wall temperature varied between calculations. One can immediately see that the ANL/AF model fails to represent the experimental data accurately, for it overpredicts the deposition rate at low temperatures while underpredicting the deposition rate at higher temperatures. Annoyingly, the predicted deposition rate starts falling at a wall temperature of ~ 625 K whereas the experimental data indicate a monotonically increasing deposition rate with temperature. These inaccuracies in the prediction can be justified when examining some particulars of the model.

Recall that one of the differences between the calibration experiments and the Purdue experiment dealt with air sparging. While the calibration experiments were constantly supplied with fresh fuel that had been air sparged, the Purdue experiment had no mechanism to saturate the fuel with oxygen. In fact, the Purdue test configuration tends to remove oxygen from the fuel due to the N₂ overpressure on the fuel. Furthermore, since the fuel was recirculated in the Purdue test, the oxygen content in the fuel would decrease steadily with time. Therefore, one can assume that by using the saturation value of oxygen in the model that the model predictions would overemphasize the oxidative deposition in the region below 600 K. This point is clearly demonstrated in Figure 4 where the model overpredicts the deposition rate for temperatures below 600 K.

The drop in the deposition rate at higher temperatures arises from a very different aspect of the model. Recall that two reactions occur in the bulk fuel; one to form precursors in the oxidative regime and one to eliminate precursors at high temperatures. When the temperature is sufficiently high (> 650 K), the precursor destruction reaction (Equation 2) begins to dominate the precursor formation reaction. The result of this is a steadily decreasing contribution to the wall deposition rate from the reactions in the bulk fuel. Eventually, only the wall reaction contributes to the deposition, and as the oxygen is depleted this reaction will also fail to produce appreciable deposits. Therefore, the model in its calibrated form will predict little deposition at high temperatures and no deposition at very high temperatures.

These two shortcomings of the model give rise to a new approach to simulating the Purdue data. The first step being to decrease the oxygen concentration input to the model to match the low temperature deposition data, since in this region the deposition is primarily oxidative. This change is substantiated by the difference in oxygenation of the fuel between the heated tube experiments and the Purdue Copper Block Test. The second step was to derive an additional chemistry expression to simulate a non-oxidative deposition mode that functions primarily at high temperatures. Substantiation for this change arises from a belief that the deposition mechanism changes from autooxidation to pyrolysis at ~ 700 K. This reaction provides a mechanism for deposit formation when the oxidative processes are exhausted.

The results of reducing the inlet oxygen content are given in Figure 4. It was found that an inlet oxygen concentration of 10 ppm by weight (20% of the saturation value) was required to match the low temperature (~ 570 K) deposition data. The final step in the modification of the model was to devise an additional chemistry expression to simulate deposition at high temperatures. The chosen mechanism took the following form:



This reaction represents the formation of deposit particles in the bulk fuel which contribute to the wall deposition only if diffusive and convective transport carry the particles to the wall. This reaction augments the chemistry found in Equations 1-3.

Figure 5 shows the results obtained using the modified model which is a clear improvement over its unmodified counterpart shown in Figure 4. Though the results from the modified ANL/AF model are not exceptionally good, the prediction does manage to capture the essential character of the data which indicate an increasing deposition rate with increasing wall temperature. The magnitude of the deposition rate is also reasonably accurate over a large portion of the temperature range. However, one notes that the data appears to turn downward slightly at higher temperatures while the prediction clearly turns upward. This may well indicate some error in the formulation of the chemistry which is quite likely due to the extremely simple, global nature of the chemistry model.

CONCLUSIONS

The results presented here have focused on attempts to apply a computational model for thermal stability to conditions beyond those for which it was calibrated. Attempts to model experiments which were similar to the model's calibration experiment were very successful; however, deviation from the heated tube experiments to other conditions were not met with immediate success. To reasonably predict the results of the Purdue experiment, modifications to the model input and the model itself had to be made. Clearly this indicates that errors existed in the formulation of the degradation chemistry prior to its modification. Furthermore, even after modifications were made to the model with the specific purpose of better predicting the Purdue experiment, flaws were evident in the prediction.

Unfortunately, the complexity of fuel composition precludes the modeling of the individual chemical reactions leading to degradation. This point is moot, however, since these reactions are not known. The representation of the global degradation chemistry employed by the model is both extremely simple and likely in error. Experimentation is the key to making improvements to such models by pursuing a process of continually evaluating and improving the model. Ultimate success in this endeavor will lead to models which can aid in the future design of fuel system components with minimal deleterious effects from deposition.

NOMENCLATURE

A_n	pre-exponential constant	t	time
E_n	activation energy	T	temperature
k_n	rate constant	$[\]$	denotes concentration
R	universal gas constant		

REFERENCES

1. Krazinski, J. L. and Vanka, S. P. (1989), "Development of a Mathematical Model for the Thermal Decomposition of Aviation Fuels," Argonne National Laboratory, WRDC-TR-89-2138.
2. Krazinski, J. L., Vanka, S. P., Pearce, J. A., and Roquemore, W. M. (1990), "A Computational Fluid Dynamics and Chemistry Model for Jet Fuel Thermal Stability," ASME Paper 90-GT-33.
3. Chin, J. S. and Lefebvre, A. H. (1990), "Temperature Effects on Fuel Thermal Stability," Draft copy, to be presented at the 36th ASME International Gas Turbine Conference, June 3-6, 1991.
4. Marteney, P. J. and Spadaccini, L. J. (1984), "Thermal Decomposition of Aircraft Fuel," United Technologies Research Center, NAPC-PE-143C.
5. Marteney, P. J. and Spadaccini, L. J. (1986), "Thermal Decomposition of Aircraft Fuel," *Journal of Engineering for Gas Turbines and Power* 108, pp. 648-653.

6. Marteney, P. J. (1989), "Thermal Decomposition of JP-5 During Long Duration Tests," United Technologies Research Center, NACP-PE-201C.
7. Giovanetti, A. J. and Szetela, E. J. (1985), "Long Term Deposit Formation in Aviation Turbine Fuel at Elevated Temperature," United Technologies Research Center, NASA CR-179579.
8. Giovanetti, A. J. and Szetela, E. J. (1986), "Long Term Deposit Formation in Aviation Turbine Fuel at Elevated Temperature," AIAA-86-0525.
9. Tevelde, J. A. and Glickstein, M. R. (1983), "Heat Transfer and Thermal Stability of Alternative Aircraft Fuels," United Technologies Research Center, NACP-PE-87C, Vols. I and II.

TABLE 1: Constants in the Thermal Stability Model

Index, n	Activation Energy, E_n (kcal/mole)	Pre-exponential Constant, A_n
1	30	$1.0 \times 10^{14} \text{ cm}^3/\text{mole} \cdot \text{s}$
2	35	$3.0 \times 10^{15} \text{ s}^{-1}$
3	8	$4.0 \times 10^1 \text{ cm}^4/\text{mole} \cdot \text{s}$
4	40	$1.0 \times 10^{10} \text{ s}^{-1}$

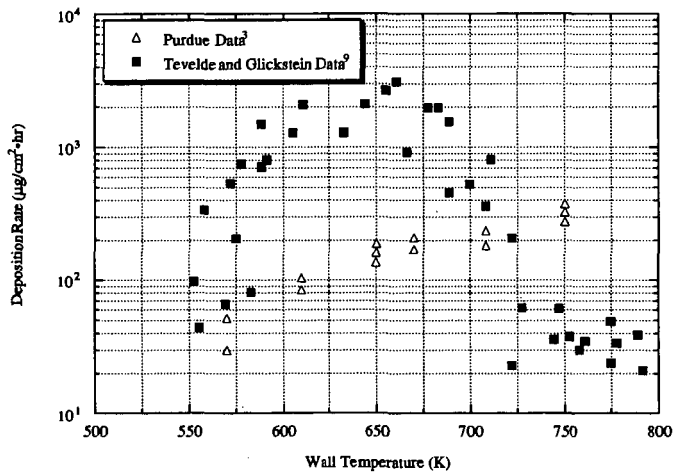


FIGURE 1: Discrepancy in the Results of Purdue and Tevelde and Glickstein

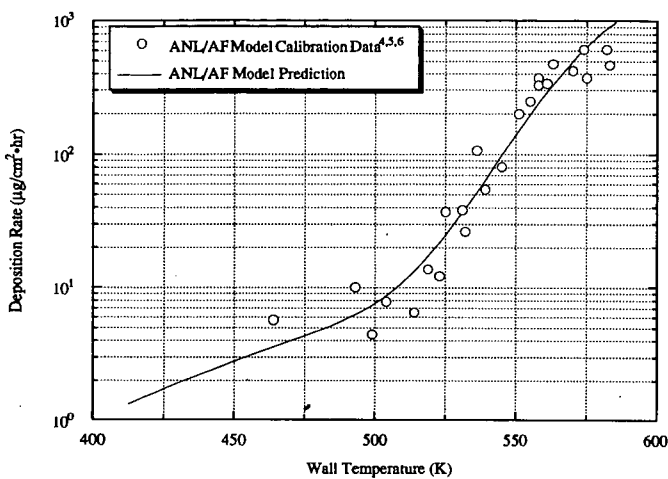


FIGURE 2: Calibration of the ANL/AF Model

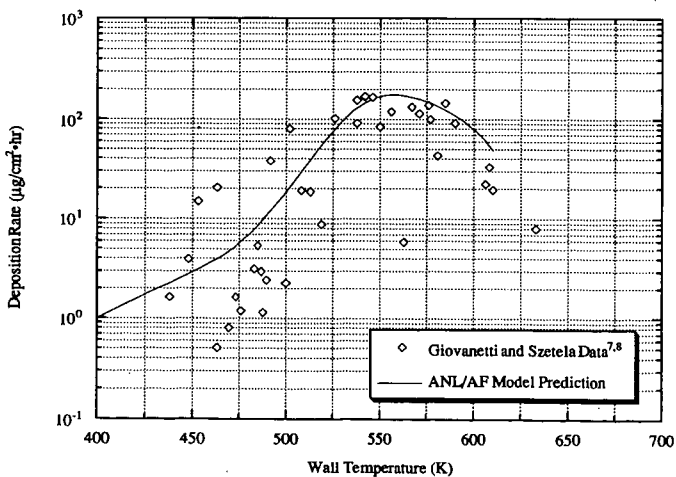


FIGURE 3: Model Calculations of Heated Tube Data

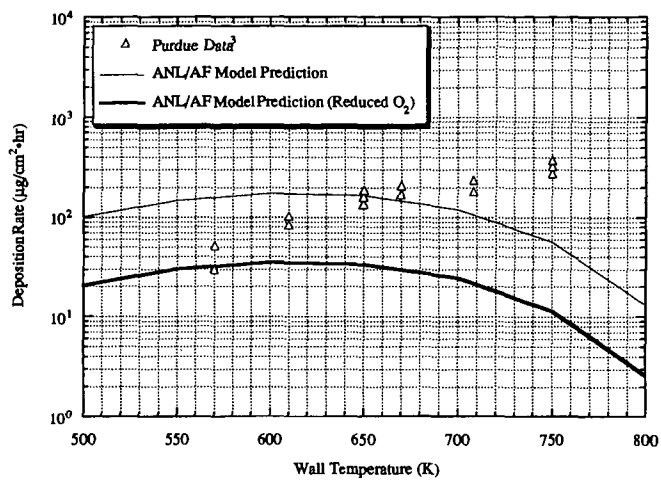


FIGURE 4: Initial Attempts to Model Purdue Copper Block Test

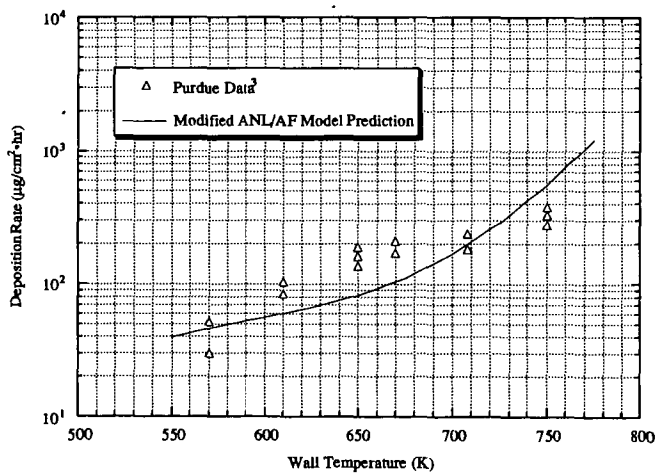


FIGURE 5: Attempts to Predict Purdue Test with Modified Degradation Chemistry

RACTAL ANALYSIS OF FUEL MOLECULES IN THE BULK LIQUID PHASE

Dennis H. Rouvray
Department of Chemistry
University of Georgia
Athens, Georgia 30602

ABSTRACT

The topological structure and boiling point of individual fuel molecules provide sufficient information for determination of their respective fractal dimensionalities in the bulk liquid phase. Molecules considered need to be members of well-defined series such as homologous series. Our fractal analysis yields a time-averaged molecular conformation for each species. The results are used to estimate the flexibility of each species in the bulk liquid phase. The presence of heteroatoms or multiple bonds in the species can produce marked effects which are alluded to in our conclusion. The present analysis elucidates the behavior of molecules in the liquid phase and sheds useful light on the physicochemical properties of many different types of fuel molecules.

Keywords: Fuel Molecules, Fractal Analysis, Molecular Behavior of Hydrocarbons

INTRODUCTION

Dwindling crude oil supplies and the many uncertainties in world oil markets render it imperative to conserve our oil resources and to utilize them as efficiently as possible. With this in mind, the method introduced here is intended to contribute to the optimal use of fuel molecules. This goal can be accomplished only after the behavior of fuel molecules at the molecular level has been thoroughly elucidated. We show here how it is possible to gain valuable insights into the average conformation of fuel molecules and analyze the factors determining these conformations. In addition, we estimate the flexibility of individual molecules in the bulk liquid phase. All this is achieved by making use of no more than the topological structures of the species under study and their experimentally measured boiling points. Although we focus here on straight-chain hydrocarbon molecules, our methodology can be readily extended to more complex species.

Our approach, originally introduced in 1986 by Rouvray and Pandey [1,2] has recently been employed in the study of species containing heteroatoms [3]. Key to the approach is the description of hydrocarbon and other chains as fractal objects; for a discussion of such objects and appropriate terminology, readers should consult standard texts [4,5]. The fractal dimensionality of each molecular chain can be related to its time-averaged conformation in the bulk liquid phase and then used to estimate the molecular flexibility. A brief mathematical exposition of the salient features of our approach now follows.

MATHEMATICAL FORMALISM

We adopt as a convenient measure for the shape of molecular chains the mean-squared end-to-end length of the species. A molecule M will satisfy a proportionality of the general type:

$$r \propto n^q, \quad (1)$$

where n is the number of atoms in the backbone of the chain, and q is typically some fractional number. An equivalent formulation in terms of the fractal dimensionality of M can also be given thus:

$$r \propto m^{1/d_f}, \quad (2)$$

Because the physicochemical properties of molecules are known [6] to depend on their time-averaged conformation in the bulk phase, we may write for some property P_i of the molecule M_i the following relationships:

$$P_i \propto r_i \propto m_i^{1/d_{fi}}. \quad (3)$$

Now, if P_i is plotted against n , or some other scalar numerical description such as a topological index [6,7], the plot can be characterized by the proportionality:

$$P_i \propto T_i^{b_i}, \quad (4)$$

where T_i is the descriptor for M_i and b_i is a constant determined from the slope of the curve at T_i . From relations (3) and (4) we can conclude that:

$$m_i^{1/d_{fi}} \propto T_i^{b_i} \quad (5)$$

The use of scaling arguments at this point, similar to those adopted by de Gennes [8], yields the final result:

$$\frac{b_1}{b_2} = \frac{d_{f2}}{d_{f1}} \quad (6)$$

for two molecules M_1 and M_2 in a given series.

RESULTS AND DISCUSSION

For simplicity, we choose for the P_i the boiling points of members of normal alkane species and for T_i the carbon number in the chain. Relevant plots on linear and logarithmic scales are shown in Figures 1 and 2 respectively. The fractal dimensionalities are obtained from the b_1/b_2 ratios by making use of the logarithmic plot; the actual values can be read off from the plot in Figure 3. Because the fractal dimensionalities provide a measure of the distribution of mass with distance [4,5], they can be used as measures of the time-averaged conformation of the species they characterize. Fractal dimensionalities for chain-like molecules all lie within the range $1 < d_f \leq 2$, with unity corresponding to a totally rigid chain. As values of d_f become progressively greater than unity they reflect the extent of folding up of the chain. Thus, for the C_1 , C_{10} , C_{20} , and C_{30} chains, the respective d_f values are 1.00, 1.18, 1.43 and 1.69.

The d_f values determined from our analysis can be employed to yield an estimate of the flexibility of each of the species in the bulk liquid phase. Our estimate is given as the product of the number of bonds in the chain, n_i-1 , and the reciprocal of the mean-squared end-to-end length of the chain, i.e.

$$F_i = (n_i-1)/r_i. \quad (7)$$

Values for F_i can be determined for any chain containing n_i atoms from our relation (3) above as follows:

$$r_i \propto m_i^{1/d_{fi}} \propto (n_i m_c)^{1/d_{fi}} \quad (8)$$

where m_c is the mass of the carbon atom ($C=12$). Substitution of appropriate values for the C_2 , C_{10} , C_{20} , and C_{30} chains leads to flexibility values of 0.042, 0.156, 0.412 and 0.900 respectively. On this measure of flexibility therefore, the C_{30} chain is roughly 21.5 times more flexible than the C_2 chain.

Our results are in accord with calculations on long alkane and other chains. Flory and Yoon [9] showed that the average shape of polyethylene chains containing 10 or more bonds may be visualized as ellipsoids. Very recent work by Erman et al. [10] has confirmed this picture and presented estimates of chain stiffness that are in broad agreement with the results presented here. Moreover, the effects of heteroatoms in the chain have been studied by us [3] as have the consequences of introducing multiple bonds into the chain. It is known that both the substitution of atoms heavier than carbon and the introduction of multiple bonds into the chain will result in a loss of flexibility or a stiffening of the chain in general [3]. This is only to be expected from the form of the expression we have used, namely relationship (7), for the computation of the chain flexibilities. Clearly, our analysis sheds much useful light on the interactions occurring at the molecular level in the bulk liquid phase. It is hoped that similar analyses in the future can be adapted for the design and optimization of fuel molecules.

REFERENCES

- [1]. D. H. Rouvray and R. B. Pandey, *J. Chem. Phys.* **85**, 2286 (1986).
- [2]. D. H. Rouvray, in *Graph Theory and Topology in Chemistry*, ed. R. B. King and D. H. Rouvray (Elsevier, Amsterdam, 1987), p. 17.
- [3]. D. H. Rouvray and H. Kumazaki, *J. Math. Chem.* in press.
- [4]. B. B. Mandelbrot, *The Fractal Geometry of Nature* (Freeman, San Francisco, 1982).
- [5]. P. Pietronero and E. Tossati, eds, *Fractals in Physics* (North Holland, Amsterdam, 1986).
- [6]. J. K. Labanowski, I. Motoc and R. A. Dammkoehler, *Computers Chem.* **15**, 47 (1991).
- [7]. D. H. Rouvray, *Scientific Am.* **255**, 40 (1986).
- [8]. P.-G. de Gennes, *Scaling Concepts in Polymer Physics* (Cornell University, Ithaca, New York, 1979).
- [9]. D. Y. Yoon and P. J. Flory, *J. Chem. Phys.* **61**, 5366 (1974).
- [10]. B. Erman, I. Bahar, A. Kloczkowski and J. E. Mark, *Macromolecules* **23**, 5335 (1990).

FIGURES

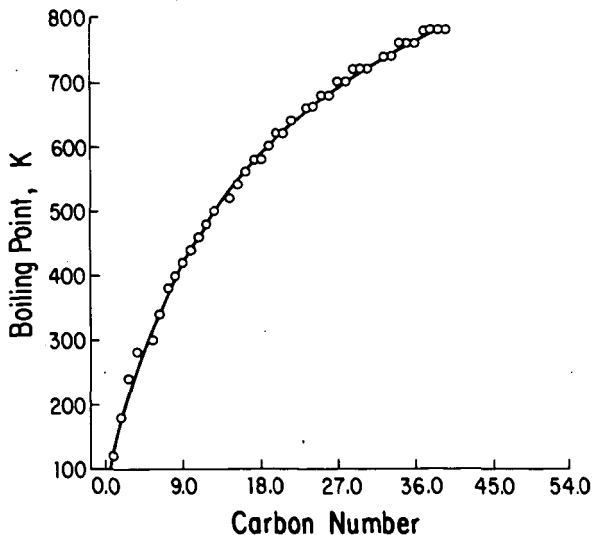


Figure 1. Plot of boiling point against carbon number on linear scales for the first forty normal alkanes.

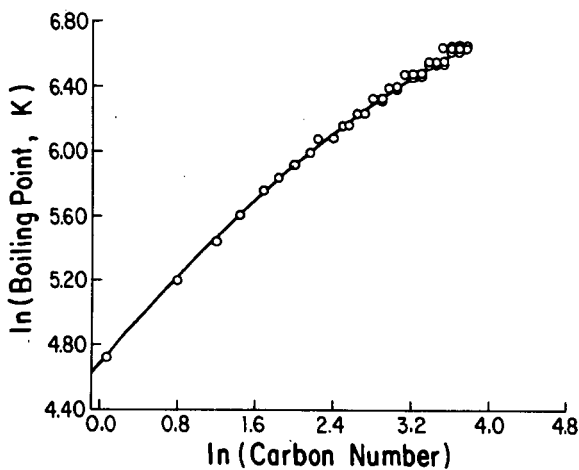


Figure 2. Plot of boiling point against carbon number on logarithmic scales for the first forty normal alkanes.

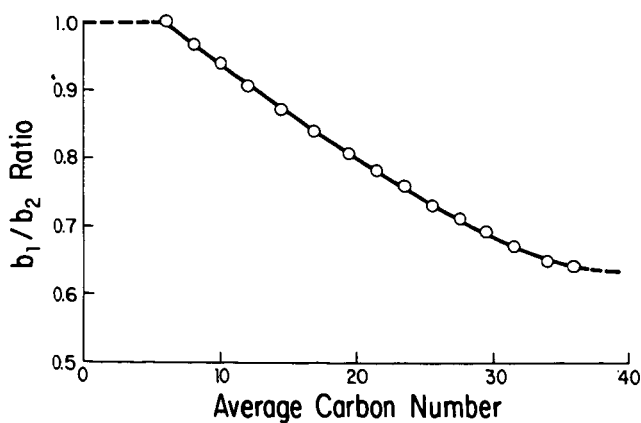


Figure 3. Plot of the b_1/b_2 ratio against carbon number on linear scales for the first forty normal alkanes.

DEVELOPMENT OF A MOLECULAR MECHANICS FORCE FIELD FOR CLAYS I. STRUCTURE AND IR SPECTRUM OF KAOLINITE

Alan G. Stellpflug, John B. Nicholas, Kathleen A. Carrado,
Glenn L. Keldsen, and Randall E. Winans
Chemistry Division, Building 200
Argonne National Laboratory
Argonne, IL 60439

Keywords: Molecular Mechanics, Force Field, Clays, Kaolinite

INTRODUCTION

The use of layered inorganic silicate clays as catalysts remains technologically vital to industry¹. It is therefore important to understand the chemistry involved with these compounds. Comprehension of the structure and dynamics of the material, how other ions and molecules interact with the clay, and the reaction mechanisms involved in the catalysis process are all critical issues. Molecular modeling techniques, encompassing energy minimization or molecular mechanics², normal mode analysis, molecular dynamics, and computer graphics, is a valuable tool for examination of these properties.

The purpose of this work was to apply molecular modeling techniques to the study of silicate clays to determine their structure and dynamics. Previous studies of related materials^{3,4,5} suggested that the results obtained would be of sufficient accuracy to compare to experiment. In addition, more accurate, *ab initio* calculations on such large molecules are nearly impossible at the present time, even on large supercomputers.

THEORETICAL METHODS

Atomic Coordinates

Our modeling efforts begin with kaolinite, an important and common clay mineral from the Kaolin or Kandite group⁶. This class of minerals is made up of a single Si(Al, Fe)-O tetrahedral sheet linked to a single Al(Mg, Fe)-OH octahedral sheet in regular succession, as displayed in Figure 1. As such, these clays are also called 1:1 minerals.

Atomic coordinates were taken from Young and Hewat's Rietveld refinement⁷ of both X-ray and neutron powder diffraction data. This refinement was chosen because Young and Hewat measured the most crystalline material available and gave definitive positions for the inner-hydroxyl hydrogen atoms. A space group of P1 was used for this refinement and the resulting cell parameters appear in Table I. The reported values, which were used for this model, must however be viewed with some caution, since aspects^{7,8,9} about the actual space group and cell parameters are still being questioned, sixty years after the idealized structure was proposed by Pauling¹⁰. The major argument about the structure seems to be whether or not the hydrogen atom positions of the inner-hydroxyls are c-face centered. The reason for many of these disputes is that available crystals of kaolinite have not been sufficiently large or coherent enough to allow good single crystal analysis¹¹.

Peak assignments for comparison to the theoretical infrared (IR) spectrum of kaolinite were taken from a compendium of data on layered materials¹². Several infrared spectra for kaolinite from different parts of the world and of different purities are contained in this source. To remain consistent with Young and Hewat⁷, who used kaolinite from Keokuk, Iowa, the IR spectrum of the Keokuk kaolinite was used.

Simulation

The simulation system was formed by several replications of the unit cell. A 4x2x3 arrangement giving a cell containing 816 atoms and having the dimensions 19.89Å x 17.86Å x 22.16Å was used for the molecular dynamics calculations. Periodic boundary conditions were used to simulate the effects of an infinite lattice framework. The non-bonded interatomic interactions were evaluated for all atoms within a cut-off radius of 8.93Å.

Non-bonded Lennard-Jones and electrostatic interactions were not calculated for atoms that were bonded (1-2 interactions) or for atoms that were involved in a bond angle (1-3 interactions), because these are accounted

for by the bond stretch and bond angle bend potentials. The method of conjugate gradients¹³ was used for the energy minimization routines. The molecular dynamics calculations were done using the "leap-frog" algorithm¹⁴ to integrate the equations of motion.

Force Field

Molecular modeling techniques that are based on classical mechanics require a force field to describe inter- and intra-molecular interactions. The force field used in this work is represented by the sum of potential energy terms:

$$V = V_s + V_\theta + V_{nb}$$

where V_s is the potential caused by bonds stretching from their equilibrium positions, V_θ is the potential related to the bending of bond angles from their equilibrium positions, and V_{nb} is the potential associated with non-bonding interactions.

Force parameters used in the potential energy terms can be calculated several ways. Quantum mechanical calculations on small molecules that mimic the clay structure can be used to determine force constants, equilibrium geometries, and charge densities. Fitting the force parameters to existing experimental data, such as IR frequencies and crystal structures, is possible and was used to help define some of the force field parameters in this work. The equilibrium values can also be varied over a small range and plotted versus the difference in potential energies of the original structure and its minimized counter-part. This method was also used for some of the force parameters in this work.

The bond stretch potentials in the force field were based on a simple harmonic potential:

$$V(r) = (K_r/2)(r-r_{eq})^2$$

where r is the interatomic distance between atoms, r_{eq} is the equilibrium bond length and K_r is the bond stretching force parameter.

Bond angle bends were also modeled after a simple harmonic potential:

$$V(\theta) = (K_\theta/2)(\theta-\theta_{eq})^2$$

where θ is the bond angle bend, θ_{eq} is the equilibrium bond angle and K_θ is the bond angle bend force constant.

The non-bonded interactions considered were of two types. The first was the Lennard-Jones 6-12 potential

$$V(r) = B/r^{12} - A/r^6$$

where A and B are Lennard-Jones parameters taken from the MM2¹⁵ force field. The second non-bonded interaction accounted for was that of electrostatic interactions. These were modeled by a Coulomb potential:

$$V(r) = q_i q_j / \epsilon r$$

where q_i and q_j represent the charges of the atoms and ϵ is the dielectric constant. The electrostatic forces are of longer range and can be more important than the Lennard-Jones terms.

RESULTS AND DISCUSSION

An important test for the accuracy of any force field is its ability to reproduce the experimental crystal structure. Energy minimizations were performed starting with the reported crystal structure of kaolinite. The final structure after minimization was then compared to the original structure using both computer graphics and root mean square (RMS) differences (Table II) for each atomic coordinate. In Figure 2 it can be seen that the minimized geometries are very close to that of the original structure, especially for the heavier silicon and aluminum atoms. The oxygen and hydrogen atoms, which are expected to have greater freedom of movement in the actual compound, account for the major differences between the theoretical and actual crystal coordinates. It is interesting to note that the inner-hydroxyl hydrogens in the minimized structure have assumed a c-centered positioning (pointing in the same direction), which deviate from the original coordinates where they point towards

different layers in the clay. However, this may be caused by the absence of a hydrogen bonding potential in the force field. If this potential is added it may cause the hydroxyl hydrogens to point towards the tetrahedral silicon layer.

Another check for the accuracy of the model force field is the force field's ability to predict the infrared spectrum. This can be done in two ways. Normal mode analysis can be used to determine the frequencies of the vibrations of the molecule. A theoretical infrared spectrum can also be calculated from molecular dynamics. This is done by taking the Fourier transform of the total dipole correlation function¹⁶ calculated from the molecular dynamics trajectory. The intensities obtained by either method are, however, strictly qualitative because the quantum corrections needed to give accurate intensities are impractical for such a large system. The force parameters and equilibrium values used in the theoretical force field are summarized in Table III.

The theoretical and experimental¹² infrared spectra for kaolinite are compared in Figure 3. Very good correlation is found in the 14 to 24 micron region of the spectrum. According to both the literature¹⁷ and to the normal mode calculations carried out on the model structure, the peaks at 19 and 21.5 microns are due to the Si-O bond stretch. The fact that the experimental and theoretical peaks match well indicate that the Si-O parameters are correct. The experimental peak at 14.5 microns is due to the Si-O-Al bond angle bend¹⁷, however, the theoretical peak is at a slightly lower energy value (16 microns). The 8 to 13 micron range of the theoretical spectrum does not clearly exhibit all the major peaks in the experimental IR spectrum, but tentative assignments can be made. The Si-O bond stretch at 9.0 microns is calculated to occur at 8.5 microns and the theoretical peak at 10.2 microns is believed to correspond to the experimental peak at 9.9 microns. This peak, along with the band at 14.5 microns, may be due to the Si-O-Al bond angle vibration. Additional molecular dynamics calculations are being performed to adjust the force constants to achieve agreement with experiment in the 8 to 10 micron region.

CONCLUSION

A force field for the clay kaolinite has been developed that gives good results both for reproducing the experimental crystal lattice structure and the infrared spectrum. A final test for this force field will be its ability to be transferred to other 1:1 layered minerals that contain aluminum, silicon, and oxygen.

ACKNOWLEDGMENTS

The Division of Educational Programs at Argonne National Laboratory is acknowledged for providing full support for AGS. This work was performed under the auspices of the Office of Basic Energy Sciences, Division of Chemical Sciences, U.S. Department of Energy, under contract number W-31-109-ENG-38.

REFERENCES

1. Pinnavaia, T.J.; *Science* **1983**, *220*, 365.
2. Boyed, D.B.; Lipkowitz, K.B. *J. Chem. Ed.* **1982**, *59*, 269-274.
3. van Beest, B.W.H.; Kramer, G.J.; van Santen, R.A. *Phys. Rev. Lett.* **1990**, *64*, 1955-1958.
4. Mabilia, M.; Pearlstein, R.A.; Hopfinger, A.J. *J. Am. Chem. Soc.* **1987**, *109*, 7960-7968.
5. Sander, M.J.; Leslie, M.; Catlow, C.R.A. *J. Chem. Soc. Chem. Comm.* **1984**, 1271.
6. Grim, R.E. *Clay Mineralogy*; McGraw-Hill: New York, **1968**, pp. 35-38.
7. Young, R.A.; Hewat, A.W.; *Clays Clay Miner.* **1988**, *36*, 225-232.
8. Adams, J.M. *Clays Clay Miner.* **1983**, *31*, 352-356.
9. Thompson, J.G.; Withers, R.L. *Clays Clay Miner.* **1987**, *35*, 237-239.
10. Pauling, L. *Proc. Nat. Acad. Sci.* **1930**, *16*, 123-129.
11. Giese, R.F. *Reviews in Mineralogy*, Vol. 19, S.W. Bailey, Ed., **1988**, pp 30-35.
12. van der Marel, H.W.; Beutelspacher, H. *Atlas of Infrared Spectroscopy of Clay Minerals and their Admixtures*; Elsevier Scientific: New York, **1976**, pp 65.
13. Gunsteren, W.F.V.; Karplus, M.J. *J. Comp. Chem.* **1980**, *11*, 266-274.
14. Hockney, R.W. *Methods Comput. Phys.* **1970**, *9*, 136-211.
15. Allinger, N.L.; Yuh, Y.H.; Lii, J.H. *J. Am. Chem. Soc.* **1989**, *111*, 8551-8566.
16. Berens, P.H.; Wilson, K.R. *J. Chem. Phys.* **1981**, *74*, 4872-4882.
17. van der Marel, H.W.; Beutelspacher, H. *Atlas of Infrared Spectroscopy of Clay Minerals and their Admixtures*; Elsevier Scientific: New York, **1976**, pp 57.

Table I. Lattice parameters of kaolinite from Young and Hewat⁷.

$a = 5.1497 \text{ \AA}$	$b = 8.9351 \text{ \AA}$	$c = 7.3855 \text{ \AA}$
$\alpha = 91.93^\circ$	$\beta = 105.04^\circ$	$\gamma = 89.79^\circ$

Table II. Room mean square (RMS) differences between X-ray crystal data and minimized structure of kaolinite.

RMS(x): 0.024	RMS(y): 0.016	RMS(z): 0.018
---------------	---------------	---------------

Table III. Force parameters and equilibrium values used in the calculated force field of kaolinite.

O(1): oxygen in silicon-oxygen rings
O(2): oxygen between silicon and aluminum layers
O(3): oxygen in bridging hydroxyls
O(4): oxygen in terminal hydroxyls

<u>BOND TYPE</u>	<u>FORCE PARAMETER (mdyne/\AA)</u>	<u>r_{eq} (\AA)</u>
Al-O(2)	2.60	1.93
Al-O(3,4)	2.80	1.77
Si-O(1)	4.15	1.65
Si-O(2)	4.15	1.63

<u>BOND TYPE</u>	<u>FORCE PARAMETER (mdyne/deg)</u>	<u>θ_{eq} (°)</u>
O(1)-Si-O(1)	0.96	106.5
O(1)-Si-O(2)	0.96	106.5
O(2)-Al-O(2)	0.90	90.0
O(2)-Al-O(3)	0.90	90.0
O(3)-Al-O(3)	0.90	90.0
Si-O(1)-Si	0.40	146.5
Al-O(2)-Al	0.10	138.0
Al-O(2)-Si	0.40	135.0
Al-O(3)-Al	0.40	138.0
Al-O(4)-H	0.15	120.0

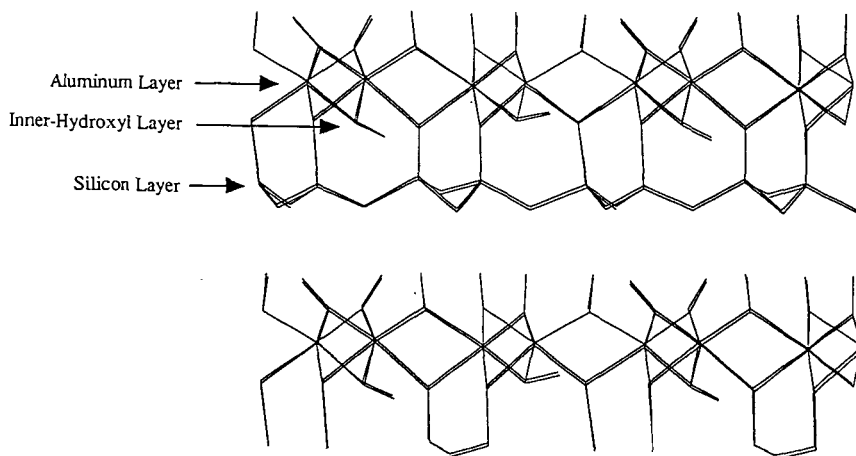


Figure 1. X-ray crystal structure of a $2 \times 2 \times 2$ lattice of kaolinite

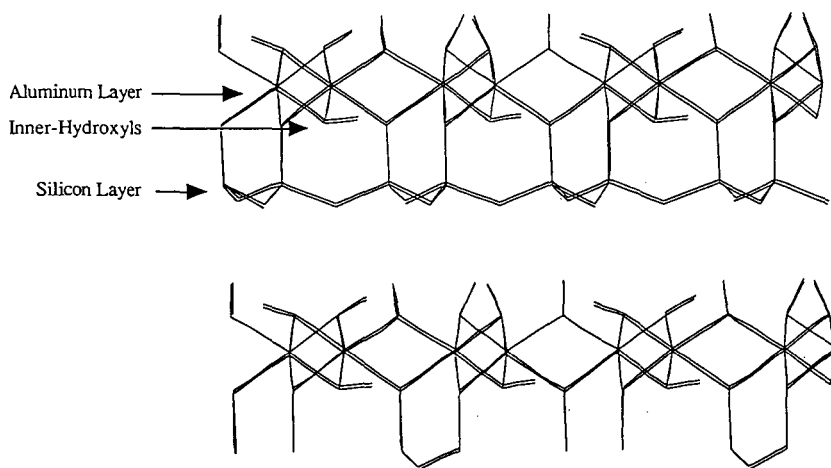


Figure 2. Minimized structure of kaolinite

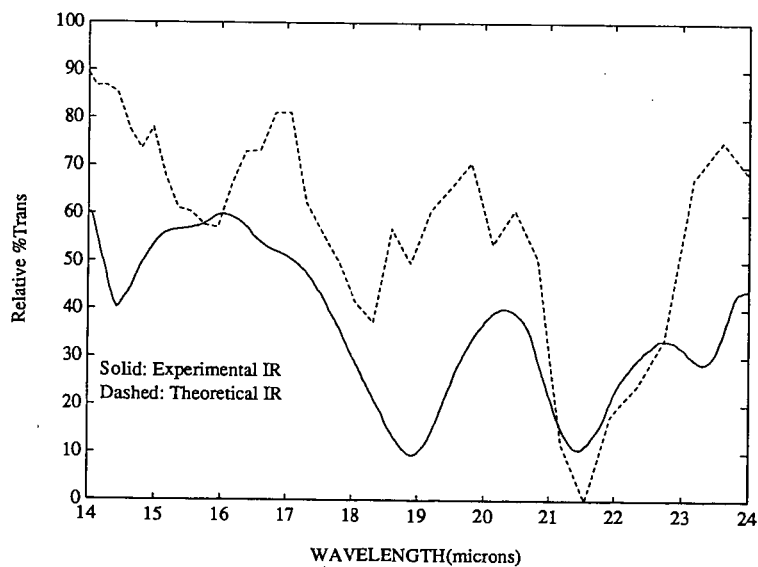
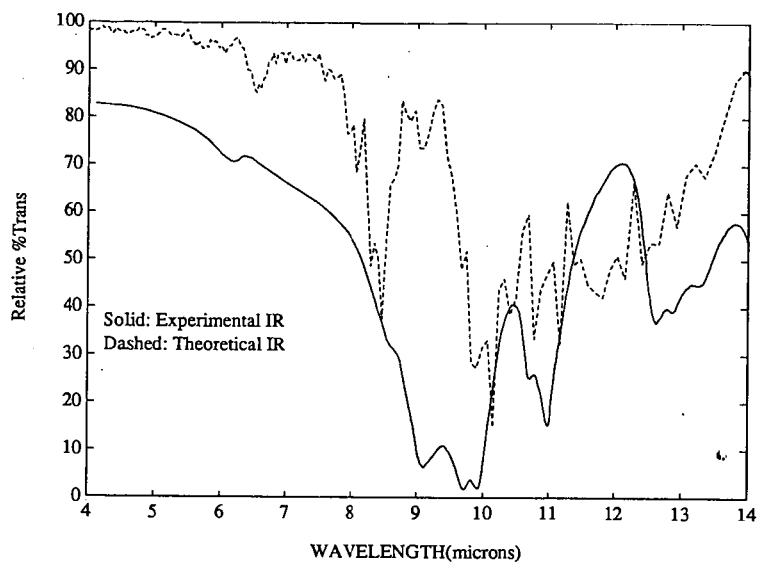


Figure 3. Comparison of theoretical and experimental infrared spectra of kaolinite

MOLECULAR MODELING STUDIES OF BITUMINOUS COAL STRUCTURE*

G. A. Carlson
Division 6211
Sandia National Laboratories
Albuquerque, N. M. 87185

Keywords: molecular modeling; computer-aided molecular design; coal structure

Abstract

Computer-aided molecular design (CAMD) has been used to define the structural conformations and intramolecular interactions of bituminous coal models. Molecular dynamics studies have produced representative minimum energy conformations for several published molecular models. These studies show the importance of van der Waals (vdW) and hydrogen-bonding interactions as cohesive forces responsible for the three-dimensional (folded) structures of the coal models. Calculations on pairs of small ring compounds representative of those found in coal clusters demonstrate that aromatics exhibit stronger vdW interactions compared with saturated ring compounds. Correlations of the vdW interactions with boiling points also show differences between aromatics and saturated rings.

Introduction

Details of coal structure and the nature of bonding within the coal structure are key concepts as one attempts to develop an understanding of coal reactivity. Because of the strong connection between structure and reactivity, there have been many studies directed toward a definition of coal structure. One group of studies has been concerned with the molecular structure of coal, as defined by various chemical and physical properties. Examples of molecular models postulated for bituminous coal are given in references 1-4. Because coal is a highly heterogeneous material, these models are only intended to be representative, or average, structures. These structures generally consist of 2-4 ring polyaromatic hydrocarbons (clusters) containing appropriate numbers of heteroatomic constituents. Most of these clusters are connected together by hydroaromatic, etheric or aliphatic linkages; others remain unconnected and relatively mobile.

The second major emphasis of bituminous coal structure studies has been to define coal as a network solid, i.e., as clusters connected together by three-dimensional cross-links (5-10). In these network models, the average size of clusters and the number of clusters between cross-links are relevant factors, while the molecular details of the clusters are relatively unimportant. Studies assuming a cross-linked structure support the concept that hydrogen bonds within the coal structure are largely responsible for defining the secondary structure of bituminous coal (6,7,9,10). The network models also explain qualitatively the observed solvent-swelling behavior of bituminous coal (6). Bituminous coals swell when intramolecular hydrogen (and perhaps other non-covalent) bonds are broken and replaced with coal-solvent hydrogen bonds. The most effective swelling solvents are those that form strong hydrogen bonds, and thus replace most or all of the original intramolecular hydrogen bonds. However, even with strong solvents, the degree of swelling is ultimately limited by the covalent cross-link structure of the coal, which is unaffected by the solvent. Thus, the extent of solvent swelling is related to the covalent cross-link density.

*This work supported by the U. S. Department of Energy and Sandia National Laboratories under Contract DE-AC04-76DP00789.

In this paper, we explore the relative importance of hydrogen bonding and van der Waals (vdW) interactions in energy-minimized coal molecular structures. While hydrogen bonding has been more widely recognized as a major contributor to the stability of middle-rank coals, vdW interactions have also been characterized as important (7,11), especially for higher-rank coals (> 87% C, daf), which contain larger, predominantly aromatic, ring systems (12). Additional support for the importance of vdW interactions in middle-rank coals is found in the work of White (13), who concluded that vdW forces were most likely the dominant intermolecular forces in liquids derived from Illinois No. 6 coal. To the extent that these liquids are similar in structure to the clusters in the coal from which they are derived, vdW interactions would be expected to be of importance for the coal as well. It has generally been found that coal-derived liquids have molecular structures similar to the parent coal (3), providing support for this view.

Method

As previously described (14), the CAMD studies were carried out using a commercial molecular modeling software program (BIOGRAF, BioDesign, Pasadena, CA), operating on a MicroVAX II computer coupled with an Evans and Sutherland PS390 graphics terminal. The CAMD software allows the construction of molecular structures of desired complexity (up to several thousand atoms) and the subsequent manipulation of those structures using molecular dynamics techniques to determine most probable (i.e., minimum-energy) structures.

The molecular dynamics calculations employ a force field model (15) that describes the potential energy of a structure in terms of interactions between covalently-bonded atoms (bond stretches, angle bends, torsions, inversions) and other, generally longer-range, interactions between non-bonded atoms (van der Waals, electrostatic and hydrogen-bond interactions). BIOGRAF uses DREIDING (16), a force field that treats a wide range of atoms and atom types.

In this paper, we focus primarily on the vdW and hydrogen bond interaction energies calculated for structures before and after molecular dynamics (energy minimization) runs. VdW interaction energies (E_{vdW}) are calculated in DREIDING using a Lennard-Jones 12-6 potential, with vdW bond strength (well depth) D_0 and equilibrium bond length R_0 defined separately for each type of atom pair.

$$E_{vdW}(R) = D_0 \cdot \left\{ \left[\frac{R_0}{R} \right]^{12} - 2 \left[\frac{R_0}{R} \right]^6 \right\} \cdot S \quad 1)$$

A switching function S is employed to gradually "cut off" the vdW calculations for atom pairs more than 8 angstroms apart. Separate calculations showed that using this cutoff affected the calculated vdW energies by 3% or less, while reducing the time required for the calculations by 4-7 times for the structures being studied (for example, for the modified Shinn structure, containing 1040 atoms, over 500,000 vdW interactions must be calculated in the absence of a distance cutoff. With a cutoff between 8 and 9 angstroms, the number of vdW interactions calculated is reduced to ~75,000).

Hydrogen bond interaction energies (E_{hb}) are calculated using a Lennard-Jones 12-10 potential with an additional dependence on the angle between acceptor atom (A), hydrogen atom (H), and donor atom (D).

$$E_{hb}(R) = D_0 \cdot \left\{ 5 \left[\frac{R_0}{R} \right]^{12} - 6 \left[\frac{R_0}{R} \right]^{10} \right\} \cdot \cos^2(\theta_{AHD}) \cdot S \quad 2)$$

All oxygen, nitrogen and sulfur atoms are considered to be potential hydrogen bond acceptors and donors. For all atom types, the equilibrium distance R_0 between donor and acceptor is defined to be 2.75 angstroms, and the equilibrium hydrogen bond strength D_0 is fixed at 9.50 kcal/mol. Since DREIDING uses the same force constants for all hydrogen bonds independent of atom types, energy calculations can be compared for one structure relative to another (providing the relative numbers of heteroatoms are similar, as in the present case), but are not accurate in absolute terms.

Calculations of hydrogen bonding and vdW interaction energies were carried out for three molecular models of bituminous coal, those of Wiser (2), Solomon (3), and Shinn (4), modified as previously described (17). Stabilization energies were determined as the differences in vdW and hydrogen bonding energies for the energy-minimized structures (after molecular dynamics calculations) relative to the initial structures. VdW interactions were also calculated for pairs of simple ring compounds ranging in size from C_6 (benzene and cyclohexane) to C_{24} (coronene and perhydrocoronene). The range of sizes and the extremes of fully-aromatic to fully-hydrogenated molecules were intended to cover the range of molecular cluster sizes and compositions believed to be present in bituminous coal. In each case, two molecules (e.g., two benzenes) were first separated by a sufficient distance to eliminate any intermolecular vdW interactions (~ 20 angstroms), and the total (intramolecular) vdW energy of the two molecules calculated. The molecules were then allowed to attain a minimum-energy configuration and the vdW energy again calculated. The difference in the two energies was taken to represent the vdW stabilization energy per molecular pair.

Results

Table I shows data related to hydrogen bond formation for each of the models studied. The total number of potential hydrogen bond donors and acceptors for each structure is given, as well as the actual number of intercluster hydrogen bonds formed in the energy-minimized molecular structures. Some additional intracluster hydrogen bonds were observed (i.e., hydrogen bonds between acceptors and donors present on the same cluster, on either the same or adjacent rings), but these do not contribute stability to the folded structure. Interestingly, although the Wiser model had the highest number of donors and acceptors relative to the total number of atoms, it exhibited the least intercluster hydrogen bonding. This was apparently because the donors and acceptors in the Wiser model are most often in close proximity, and preferentially form intracluster hydrogen bonds. The observation may also be partly due to the generally higher degree of cross-linking between clusters observed for the Wiser structure. This strong cross-linking appears to have limited the freedom of the clusters to move relative to one another, and thus may have restricted the access of intercluster donors and acceptors to each other. The average energy calculated for the intercluster hydrogen bonds for all models ranged from 4.5 to 7.9 kcal/mol, in good agreement with Larsen's data based on solvent swelling interactions (5-8.5 kcal/mol, ref. 6). The calculated values are somewhat lower than the maximum calculated bond strength (9.5 kcal/mol, Eq. 2), reflecting less than optimal hydrogen bond angles and bond lengths.

The number of vdW interactions in the energy-minimized structures and the vdW stabilization energies are also given for each model. The stabilization energy was calculated as the difference between the vdW energy of the initial structure and of the energy-minimized structure. As shown, although the number of vdW interactions for each structure is quite large (even with the assumed vdW cutoff distance), the energy per interaction is very small (~ 0.005 kcal).

Finally, the differences between the vdW and hydrogen bond energies for each model before and after energy minimization were compared, to evaluate their relative contributions to stabilization of the secondary structure. As Table I shows, the vdW stabilization energy was in every case greater than that due to hydrogen bond formation by roughly a factor of 2-3. It is not obvious how to compare the relative importance of vdW and hydrogen bonding interactions based on these total energy data, which sum up tens of thousands of vdW

interactions but only tens of hydrogen bonding interactions. However, it does seem clear from these data that vdW interactions are significant contributors to bituminous coal structural stability.

To further evaluate the significance of vdW interactions in coal, vdW interactions were calculated for pairs of simple aromatic and saturated-ring compounds ranging in size from C_6 (benzene and cyclohexane) to C_{24} (coronene and perhydrocoronene). Figure 1 shows the vdW stabilization energies for each molecular pair, normalized to the number of carbon atoms in each molecule and plotted against the molecular weight of the molecule. For the aromatic molecules, there is a well-defined progression toward greater stabilization energy (per carbon atom) with ring size. This is to be expected, since there are more vdW interactions possible for larger molecules. By contrast, for the fully-saturated rings, the vdW stabilization per carbon tends to be smaller than for the aromatics and is relatively unchanged with ring size. Apparently the steric overlap of the non-planar hydrogens in the saturated ring compounds prevents the molecular pairs from approaching to optimal distances for C-C vdW interactions (the C-C distance for equivalent carbons in the aromatic ring pairs is ~ 3.5 - 3.7 angstroms, relatively near to the equilibrium vdW C-C distance of 3.9 Angstroms; for the saturated ring pairs, the C-C distance ranges from 4.7 - 5.1 angstroms).

These calculations may overestimate somewhat the vdW interactions for the aromatic ring compounds. The calculated minimum-energy conformations for all the molecular pairs are with rings in a face-to-face parallel configuration. However, Larsen has reported that quadrupole interactions for aromatic ring compounds (which are not calculated in most force field approximations) are repulsive for a parallel ring configuration, and tend to force rings to orient in a perpendicular (T-shaped) fashion (18). The tendency to form non-planar pairs is strongest for small rings (e.g., benzene), and weakest for large rings. If quadrupole effects were included, vdW interactions for benzene might be reduced by roughly 50%, but for coronene by less than 20% (19). Thus, the actual progression of vdW stabilization energy with size for aromatic ring compounds would likely be even more pronounced than Fig. 1 indicates. The effects of quadrupole interactions on the orientation of saturated ring pairs are not known.

Figure 1 also shows the vdW stabilization energies for the three coal structures previously discussed, expressed in terms of the average molecular cluster size. The average molecular cluster size for each structure was obtained after dividing the structure into "clusters" at apparent linkage sites (aliphatic, etheric bridges, etc.). These coal structure stabilization energies represent all the interactions of the molecular clusters, not just those of pairwise clusters. The tendency of the coal structure stabilization energies to be somewhat lower than the pairwise molecular interaction energies is believed to reflect the constraints of the covalent bonds between coal clusters, which tend to prevent fully-optimal ring overlap.

In earlier studies of hydrocarbon liquids, White found an excellent correlation between boiling point data and gas-chromatographic retention indices for 48 polyaromatic hydrocarbons (20). Such correlations are of value when evaluating the boiling fractions derived from coal liquefaction products. In this work, White did not consider partially- or fully-saturated ring compounds, which also would be important constituents in liquids from coal. Boiling points reflect generally the intermolecular forces, including vdW interactions, between molecules. In Fig. 2, the boiling points for the molecules represented in Fig. 1 (excluding perhydrocoronene, for which data were not found) are plotted against the vdW stabilization energies. The data separate into two quite distinct, relatively linear sets, one for aromatic and one for saturated ring compounds. Additional data would be necessary to determine whether such correlations are sufficiently accurate to provide predictive value for other ring compounds.

Discussion

Calculations of bituminous coal structures using CAMD techniques have demonstrated that intercluster vdW and hydrogen-bond interactions provide significant energy stabilization, with

vdW interactions apparently providing a larger total contribution to stabilization. The importance of vdW interactions for middle-rank coals has been pointed out previously (7,11), but not the possibility that vdW interactions actually may contribute more to energy stabilization than hydrogen bonds. The present calculations based on pairs of ring compounds show the relative effects of ring size and of ring saturation on vdW stabilization energy. These data support the increased strength of vdW interactions reported for higher-rank coals (11,12), for which the average ring size and the degree of aromaticity both increase. The ring pair data also have been shown to correlate reasonably well with boiling point data for a limited range of molecules, with aromatic ring compounds showing a distinctly different relationship than saturated ring compounds. It would be interesting to study partially-saturated rings and heteroatom-containing ring compounds as well, to provide additional data for comparison with coals and coal products.

The present studies were based on molecular models of coal, which do not incorporate the three-dimensional cross-linking that is believed to occur in actual coal structures. To address this issue, CAMD studies of coal as a network structure are planned. In these studies, representative molecular clusters (modified relative to the molecular structures considered in this work, to account for more recent chemical and structural data, refs. 21-23) will be linked together with intermittent cross-links, forming a three-dimensional structure. The structures will be energy minimized, and vdW and hydrogen bond interactions evaluated. Also, the physical density represented by the structures will be calculated, and the presence of void volume (microporosity) determined. Results will be correlated with various experimental data and with theoretical network models for coal.

Acknowledgements

Helpful suggestions and discussions of the van der Waals studies by Malvina Farcasiu and Curtis White, Pittsburgh Energy Technology Center, are gratefully acknowledged.

References

1. Given, P. H., Fuel 1960, **39**, 147.
2. Wiser, W. H., Proc. of the Electric Power Research Institute Conf. on Coal Catalysis, 1973.
3. Solomon, P. R., in New Approaches in Coal Chemistry, Am. Chem. Soc. Symp. Series No. 169, 1981; p. 61.
4. Shinn, J. H., Fuel 1984, **63**, 1187.
5. Larsen, J. W., Am. Chem. Soc. Div. Fuel Chem. Preprints 1985, **30**(4), 444.
6. Larsen, J. W., Green, T. K., and Kovac, J., J. Org. Chem. 1985, **50**, 4729.
7. Brenner, D., Fuel 1985, **64**, 167.
8. Solomon, P. R., Best, P. E., Yu, Z. Z., and Deshpande, G. V., Am. Chem. Soc. Div. Fuel Chem. Preprints 1989, **34**(3), 895.
9. Hall, P. J., Marsh, H. and Thomas, K. M., Fuel 1988, **67**, 863.
10. Lucht, L. M., and Peppas, N. A., Fuel 1987, **66**, 803.
11. Mallya, N. and Stock, L. M., Fuel 1986, **65**, 736.
12. White, C. M., and Schmidt, C. E., Fuel 1987, **66**, 1030.
13. Carlson, G. A., Am. Chem. Soc. Div. Fuel Chem. Preprints 1989, **34**(3), 780.
14. Fruhbeis, H., Klein, R., and Wallmeir, H., Angew. Chem. Int. Ed. Engl. 1987, **26**, 403.
15. BioDesign, Pasadena, CA, unpublished data.
16. Carlson, G. A., "Modeling of Coal Structure Using Computer-Aided Molecular Design", to be published in the Given Symposium Advances in Coal Science series (1991).
17. Larsen, J. W., Am. Chem. Soc. Div. Fuel Chem. Preprints 1988, **33**(1), 400.
18. Miller, J. H., Mallard, W. G., and Smyth, K. C., J. Phys. Chem. 1984, **88**, 4963.
19. White, C. M., J. Chem. Eng. Data 1986, **31**, 198.
20. Solum, M. S., Pugmire, R. J., and Grant, D. M., Energy & Fuels 1989, **3**, 187.
21. Carlson, R. E., Brigham Young University, unpublished data.
22. Winans, R. E., Argonne National Laboratory, unpublished data.

Table I

HYDROGEN BONDS AND VAN DER WAALS INTERACTIONS IN COAL STRUCTURES

<u>Parameter</u>	<u>Wiser</u>	<u>Solomon</u>	<u>Shinn</u>
<u>Total # Atoms</u>	394	396	1040
<u>Hydrogen Bonds</u>			
# H-Bond Acceptors	26	20	68
# H-Bond Donors	16	12	30
# Intercluster H-Bonds Formed	5	9	29
Δ H-Bond Energy	-25	-71	-130
Energy/Intercluster H-Bond	-5.0	-7.9	-4.5
<u>Van der Waals Interactions</u>			
Total # vdW Interactions	20451	21706	74882
Δ vdW Energy	-84	-119	-341
Energy/vdW Interaction	-.004	-.005	-.005
<u>Energy Comparison</u>			
Ratio $\frac{\Delta \text{ H-Bond Energy}}{\Delta \text{ vdW Energy}}$.30	.60	.38

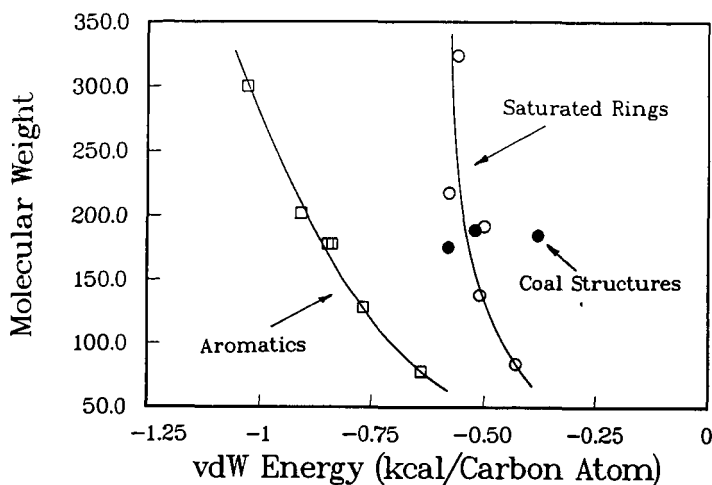


Fig. 1. Van der Waals stabilization energies for pairs of aromatics and saturated ring compounds as a function of molecular weight, and for bituminous coal structures as a function of cluster size. Lines are hand fits to data, drawn to aid the eye.

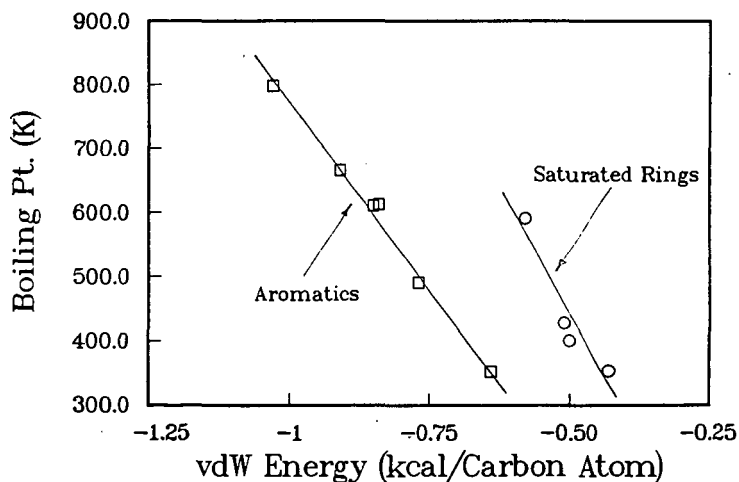


Fig. 2. Van der Waals stabilization energies for pairs of aromatics and saturated ring compounds, plotted as a function of boiling points. Straight lines are hand fits to data, drawn to aid the eye.

AN ALTERNATIVE TO "STERIC C-H COMPRESSION" AS THE SOURCE OF UPFIELD CARBON-13 NMR SHIFTS IN POLYMETHYLARENES.

Brian M. Lynch

Department of Chemistry, St. Francis Xavier University
Antigonish, Nova Scotia B2G 1C0, Canada

KEYWORDS: Carbon-13 nmr, steric extension, C-C bond lengths, MM2 calculations
INTRODUCTION

Vicinal alkyl groups attached to benzenoid rings or cycloalkane moieties in a tetralin-like configuration are commonly postulated features in structural models of bituminous coals [for examples, see [1]]. Formation of cyclic carboxylic acid anhydrides (analogous to phthalic anhydride) from mild oxidations of such coals [2] is one item of evidence in support of this postulate, and it would be expected that features from vicinal alkyl species should be readily identifiable if highly resolved carbon-13 nmr spectra of coals were to be obtained. This expectation should be readily testable since in polymethylarenes, methyl carbon-13 nmr shift patterns are observed in which ortho-related methyl carbon signals are significantly upfield (up to 7 ppm) from those of isolated methyl groups. These patterns are usually interpreted by suggesting that non-bonded repulsion between alkyl hydrogen atoms [3-5] leads to **steric compression** of C-H bonds. Many other carbon-13 "steric shifts" are rationalized similarly, with electron migration postulated in the sense $\delta^+ \text{H-C} \delta^-$ [6,7]. However, bond length and angle distortions occur more readily for C-C bonds than for C-H bonds (compare $\nu \text{ CH}$, $\sim 3000 \text{ cm}^{-1}$; $\nu \text{ CC}$, $\sim 1000 \text{ cm}^{-1}$, and $\delta \text{ CH} \sim 1450 \text{ cm}^{-1}$; $\delta \text{ CC} \sim 700 \text{ cm}^{-1}$), so hydrogen-hydrogen repulsions are not likely to be the only significant steric factors. Further, the methyl proton shifts in ortho-xylene are also upfield from those in the meta and para isomers [8].

PROCEDURES AND DISCUSSION

I have tested the validity of the **steric compression** postulate, using Allinger's MM2 force field approach [9] with the commercial application Chem3D Plus™ [10] on a Macintosh II microcomputer. I calculated equilibrium geometries of various methylarenes (benzenes, naphthalenes, anthracenes). The steric interactions were minimized iteratively, considering contributions from compression-stretching, bending, stretch-bend, van der Waals, dipole-dipole, and torsional forces. Ten to one hundred iterations are sufficient to reach self-consistent minima. Calculations for ten distinct environments for methyl groups suggest (see Table 1) that the major variations in geometry minimizing non-bonded repulsions are bond extensions of the aryl C - alkyl C bonds, and appropriate angular changes.

Bond length and angle distortions occur more readily for C-C bonds than for C-H bonds, consistent with the appropriate force constants.

The methyl carbon-13 shifts are linearly correlated with aryl C - alkyl C bond lengths: shift increases as bond length decreases (Figure 1). The hybridization of the alkyl carbons is unchanged; one-bond carbon-13 - proton coupling constants are within 0.5 Hz of 125 Hz.

I interpret these results as decreased hyperconjugative interactions between the methyl groups and the attached aromatic species with increasing aryl C - alkyl C bond length, and as a direct consequence, decreased C-methyl carbon-13 shifts. In this series of compounds, there is **steric extension** of carbon-carbon bond lengths to avoid the hydrogen-hydrogen repulsions in the steric compression model proposed by Grant and coworkers.

This is not to discount the possible significance of non-bonded hydrogen-hydrogen repulsion effects under appropriate circumstances. In the polycyclic aromatic phenanthrene a similar MM2 treatment may be applied to deduce the preferred geometry. In this species, the two hydrogens of the C-H bonds in a bay environment are shortened significantly, but the major predicted changes are systematic deformations of the entire ring geometry and bending of the bay C-H bonds with increased angles. The predicted C-C bond lengths in the phenanthrene skeleton show excellent correlations with those observed from neutron diffraction measurements (see Figure 2).

ACKNOWLEDGEMENTS

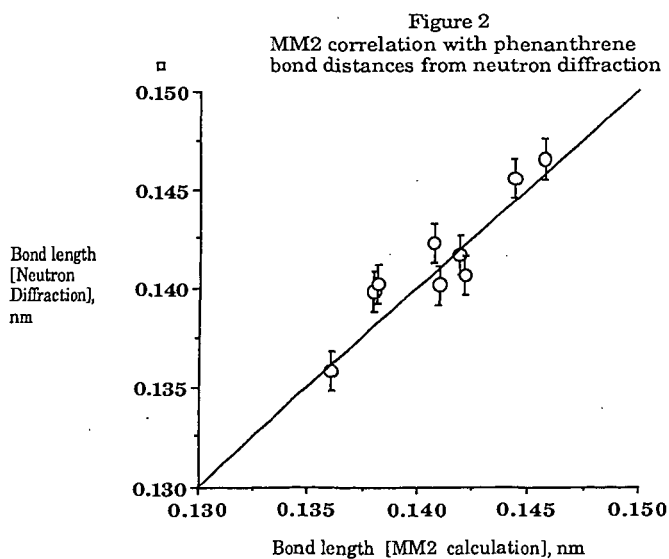
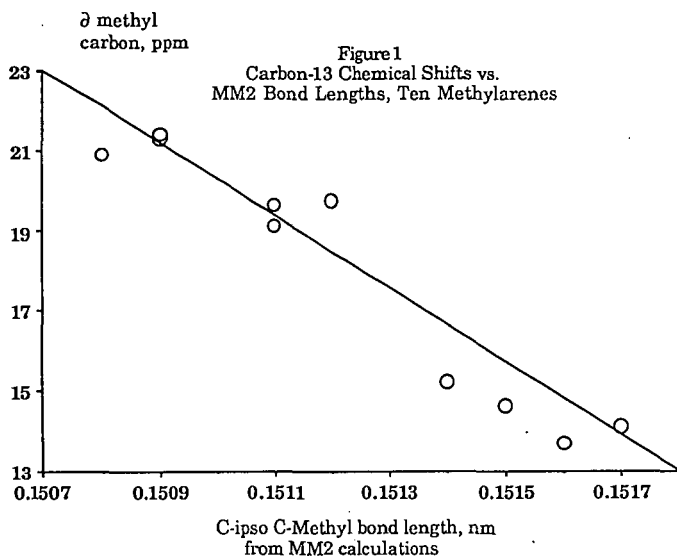
This work was catalysed by an opportunity provided by a Project SERAPHIM Fellowship held in summer 1988 at the Department of Chemistry of Eastern Michigan University, Ypsilanti, Michigan. Thanks are accorded for this award.

REFERENCES

1. Davidson, R. M. in Gorbaty, M. L.; Larsen, J. W.; Wender, I., Editors. Coal Science. Volume 1. Molecular Structure of Coal. Academic Press, 1982.
2. Lynch, B. M. and MacPhee, J. A. in Nelson, C. R., Editor. Chemistry of Coal Weathering (Coal Science and Technology 14). Elsevier, Amsterdam, 1989, p. 93.
3. Woolfenden, W. R.; Grant, D. M. J. Am. Chem. Soc. 1966, 88, 1496.
4. Grant, D. M.; Cheney, V. B. J. Am. Chem. Soc. 1967, 89, 5315.
5. Dalling, D. K.; Grant, D. M. J. Am. Chem. Soc. 1967, 89, 6612.
6. Perlin, A. S.; Casu, B.; Koch, H. J. Can. J. Chem. 1970, 48, 2599.
7. Dorman, D. E.; Roberts, J. D. J. Am. Chem. Soc. 1970, 92, 1355.
8. Bhacca, N.S.; Johnson, L. F.; Shoolery, J. N. NMR Spectra Catalog. Varian Associates, Palo Alto, California, 1962. Spectra 201-203.
9. Berkert, U.; Allinger, N. L. Molecular Mechanics. American Chemical Society: Washington, D. C., 1982.
10. Cambridge Scientific Computing, Inc., Cambridge, Mass. 02139.

Table 1
Carbon-13 shifts for methyl groups in methylarenes

Compound	Shift, ppm	MM2 bond length, nm
Toluene	21.3	0.1509
o-Xylene	19.6	0.1511
9-Methylantracene	13.7	0.1516
9,10-Dimethylantracene	14.1	0.1517
1,2,3-trimethylbenzene	15.2 (2)	0.1514
1-Methylnaphthalene	19.1	0.1511
1-Methylantracene	19.7	0.1512
2-Methylnaphthalene	21.4	0.1509
1,2,3,5-tetramethylbenzene	14.6(2)	0.1515
	20.9(5)	0.1508



DEVELOPMENTS IN SIMULATION METHODS FOR SOLID CATALYSTS

C. M. Freeman, A. T. J. Hope, S. M. Levine,
J. M. Newsam, J. Sauer, R. F. Smith and S. Tomlinson

BIOSYM Technologies Inc.
10065A Barnes Canyon Rd., San Diego CA 92121

Keywords: Computer simulation, Catalyst characterization, Catalyst structure

INTRODUCTION

The complexity of most heterogeneous catalyst systems has traditionally hampered the effective application of computer simulation methods. However, increasing sophistication in methodology and application, coupled with the development of tools specifically tailored for solid catalyst systems is now enabling computer modeling to address a number of problems encountered during the development and implementation of a variety of heterogeneous catalysts. We outline here some of our recent progress in this area, and give specific examples taken from (1) the characterization of crystalline catalysts and supports (2), the development and dynamical simulation of metal atoms and clusters on amorphous inorganic matrices (3), the dynamical behavior of hydrocarbons within microporous media and (4) the application of quantum chemical tools to studying local coordination environments and chemistries. In-depth theoretical studies of reaction pathways over real, multicomponent heterogeneous catalysts at process conditions remain a far distant goal, but, as the present examples demonstrate, considerable insight can be gleaned when tailored tools and approaches are applied to appropriately phrased heterogeneous catalyst problems.

CATALYST CHARACTERIZATION

Structural characterization is a key step in the development of a fundamental understanding of catalyst function. Most real heterogeneous catalyst systems are, however, complex and do not lend themselves readily to study by conventional structural characterization tools. Microporous crystals such as zeolites, the basis for current fluid cracking catalysts, and mixed metal oxides of interest in a wide range of oxidation reactions are microcrystalline. Powder X-ray diffraction techniques are therefore a key source of structural data. Powder diffraction data can, using the Rietveld method, be the basis for refinement of an approximate model, but the derivation of the initial model is often difficult. Computer simulations can greatly facilitate the structure solution process, either by direct derivation of an initial model from unit cell and compositional data, combined with established geometrical constraints (1), or by enabling a developing structural model to be manually adjusted while the degree of match between the simulated powder diffraction pattern and that observed is interactively monitored (Figure 1) (2, 3).

AMORPHOUS SUPPORTS

Heterogeneous catalysts are rarely used in a 'neat' form and in many cases the catalyst support or binder can play a significant role in processes. For example, classical reforming catalysts, or a large number of hydrogenation catalysts are comprised of metals dispersed on non-crystalline supports. In such cases a direct determination of structure from scattering data is not possible. Computer simulations can, however, be used effectively to develop models for the surfaces of amorphous

matrices, such as silica (4), and to study the dynamical interactions of metal atoms and clusters with such a support (Figure 2) (5, 6).

HYDROCARBONS WITHIN MICROPOROUS CRYSTALS

The behavior of hydrocarbons within microporous crystals such as zeolites is central to the role of zeolites as catalysts and sorbents. A number of experimental tools can be applied to studying the preferred sites occupied by sorbed hydrocarbons within zeolites, and aspects of the character of the hydrocarbon molecular motion over several time-scales (7). Modeling is already being applied in studies of sorbate location and diffusion (e.g. (2, 8, 9)), and computer simulations will clearly play an increasingly important role as the mechanism by which the experimental insights provided by these various methods can be combined into a self-consistent picture of the zeolite - hydrocarbon interactions. Key areas for development are the potential functions and parameters used in describing the interatomic interactions, and methods for simulating dynamical phenomena that occur on characteristic time scales longer than a few thousand picoseconds for which classical molecular dynamics methods are currently unviable.

APPLICATIONS OF QUANTUM CHEMICAL METHODS

Quantum chemical methods must play a central role in developing an understanding of catalyst reactivity. However, the complexity of real catalysts that hampers the application of structural characterization methods also imposes restrictions on the degree to which quantum chemical methods can be applied to models that approximate actual catalyst centers. Methods are continually being refined and *ab initio* Hartree-Fock calculations on a complete sodalite cage have recently been described (10). *Ab initio* methods have also contributed considerably to our understanding of Brønsted acidity in zeolites and to the geometries of such active sites (11, 12). Additionally, *ab initio* methods provide a powerful means of computing potential energy surfaces and of hence deriving potential energy functions and parameters for both intra- and intermolecular interactions.

ACKNOWLEDGEMENTS

The BIOSYM Catalysis and Sorption project is supported by a consortium of member companies.

LITERATURE CITED

- (1) Deem, M. W.; Newsam, J. M. *Nature* 1989, 342, 260-262.
- (2) Freeman, C. M.; Catlow, C. R. A. *Chem. Ind.* 1990, 3, 796-799.
- (3) BIOSYM Technologies Inc, Catalysis and Sorption Project Software (1991).
- (4) Levine, S. M.; Garofalini, S. H. in *Surface structure of silica glasses by molecular dynamics simulations*; Materials Research Society, Pittsburgh, PA, 1986; pp 29-37.
- (5) Levine, S. M.; Garofalini, S. H. *Surf. Sci.* 1985, 163, 59-66.
- (6) Levine, S. M.; Garofalini, S. H. 1990, in preparation.
- (7) Newsam, J. M.; Silbermagel, B. G.; Melchior, M. T.; Brun, T. O.; Trouw, F. in *Motion of Organic Species Occluded or Sorbed within Zeolites*; Atwood, J. L.; Plenum, New York, 1990; pp 325-337.

- (8) Newsam, J. M.; Silbernagel, B. G.; Garcia, A. R.; Melchior, M. T.; Fung, S. C. in *Structure-Activity Relationships in Heterogeneous Catalysis* (Stud. Surf. Sci. Catal.); Grasselli, R. K. Sleight, A. W.; Elsevier, Amsterdam, 1991, in press.
- (9) Schröder, K.; Sauer, J. *Chem. Phys. Lett.* 1990, 271, 289-296.
- (10) Ahlrichs, R.; Bär, M.; Häser, M.; Kölmel, C. M.; Sauer, J. *Chem. Phys. Lett.* 1989, 164, 199-204.
- (11) Sauer, J. *Chem. Rev.* 1989, 89, 199-255.
- (12) Sauer, J.; Kölmel, C. M.; Hill, J. R.; Ahlrichs, R. *Chem. Phys. Lett.* 1989, 164, 193-198.

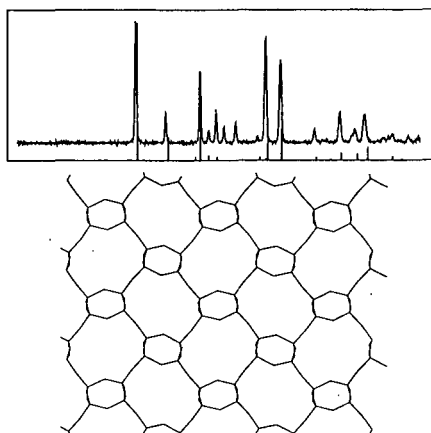


Figure 1: A model of the zeolite ABW-framework drawn as straight lines connecting adjacent Si or Al sites and their coordinating oxygen atoms (lower). The powder X-ray diffraction pattern computed interactively as the structure is edited is shown above as bars, compared with the experimental pattern of an ABW-framework material (continuous line) (3).

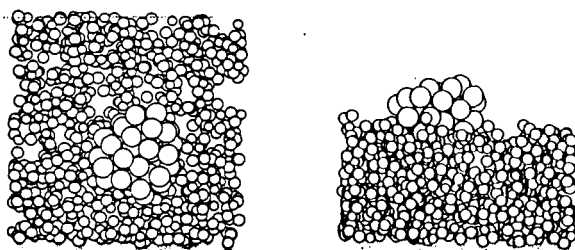


Figure 2: Top (left) and side (right) views of a model Pt cluster on a vitreous silica support generated by a series of molecular dynamics simulations (5, 6).

MOLECULAR MODELLING OF KEROGENS AND RELATED COMPOUNDS AS A TOOL FOR PREDICTION OF FOSSIL FUELS GENESIS

F. BEHAR*, M. VANDENBROUCKE* and J. L. FAULON**

* IFP, 1-4 Avenue Bois Préau, 92506 RUEIL MALMAISON, FRANCE. ** C.A.O. Robotique, Armines, 60 Boulevard St Michel, 75272 PARIS Cedex 06, FRANCE

Key-words: molecular modelling of kerogen, thermal cracking, oil, kinetics.

INTRODUCTION

Kerogen is defined as that fraction of sedimentary organic matter which is insoluble in usual organic solvents (1). It is a mixture of macromolecules whose structures evolve under the influence of time and temperature due to increasing sediment burial. Thermal cracking of kerogen (primary cracking) will lead to petroleum generation. Oil is formed first, further thermal degradation of kerogen and oil (secondary cracking) will produce gaseous compounds. Prediction of both quantity and quality of hydrocarbons generated from a given kerogen buried in a given sedimentary basin are of paramount importance as exploration guide. Thus, simulation of thermal degradation of organic matter in laboratory has been performed in order to elaborate kinetic models. These kinetic models can be really predictive only when the three following conditions are fulfilled:

1°) knowledge of chemical structure of reactants,

2°) knowledge of chemical structure of degradation products,

3°) establishment of laws relating chemical structures of reactants and products.

For many years, attention has been focused on characterization of pyrolysis products and establishment of kinetic laws, but a chemical structure was not available when kerogen, coal or heavy ends of petroleum such as resins and asphaltenes were studied. In this paper, we will present the approach we are following for modelling these complex structures and how we can relate kerogen and/or asphaltenes modelling to kinetics.

Many experimental devices have been developed for simulating thermal cracking of kerogen or asphaltenes (2). As these insoluble compounds are generally not vaporisable, experimental simulation of cracking can be done either in open pyrolysis systems swept by an inert carrier gas (3, 4, 5 among others) or in closed pyrolysis systems (6, 7 among others). An open pyrolysis system is very convenient because it allows continuous detection of effluents and programmed temperature increase. Thus, many samples can be studied in a short experimentation time. Nevertheless, transport effects due to the delay between formation and detection of effluents, can both modify kinetic parameters such as the apparent activation energies (8) and underestimate the yield of heavy compounds such as resins and asphaltenes; these latter, if they are only partially swept out of the pyrolysis chamber, can be further cracked together with the residual kerogen. Moreover, secondary cracking reactions cannot be simulated as pyrolysis products are swept away as soon as they are generated. In a closed pyrolysis system, primary cracking can be observed for low conversion yields, whereas secondary cracking will occur for higher severity, but care must be taken regarding both wall effects (9) and overlap of primary and secondary reactions. There are currently not enough available data for doing a real comparison between

open and closed systems. As the aim of our work is to elaborate a complete kinetic scheme including both primary and secondary cracking, we have chosen to perform the experimental work in a closed system.

Compounds involved in thermal cracking reactions can be identified unambiguously when present either as gaseous or liquid products. Therefore, they can be classified according to their chemical structure and carbon number, and their relative thermal stabilities can be compared.

When kerogen and heavy ends of petroleum are pyrolysed, characterization of these latter in terms of chemical bonds distribution and molecular moieties is not available. As a consequence, establishment of a predictive kinetic scheme based on chemical structure for these complex macromolecules, is not yet possible. To overcome this difficulty, we propose to use the molecular modelling software Xmol (10) which, through a combination of atomic and molecular analyses of an unknown insoluble sedimentary organic matter, builds up a self consistent 3D chemical structure. Although the 3D structural representation can be disputed, and is maybe unrealistic, it allows a correct statistical balance of all kinds of bonds present in the macromolecule. Thus, the amount and the distribution of these chemical bonds can be listed and can be related to the distribution of stoichiometric coefficients of the kinetic scheme obtained from experimental simulation.

In this paper, preliminary experimental results on kinetics of cracking of oils and kerogens will be presented. We are currently gathering all the data necessary to link kinetic scheme and molecular structure of reference kerogens.

SAMPLES

Four samples were selected: two kerogens (Type II and Type III) and two oils (Boscan and Pematang), the first one being aromatic and the second one paraffinic. As during thermal cracking each oil produces both lighter and heavier molecules than those present in the initial oil, the resulting pyrolysate will be a complex mixture of new compounds plus reactants not yet degraded. In order to discriminate between reactants and products, we have chosen to study each oil after fractionation into two classes: the first one (distillate) comprising light hydrocarbons ranging from C6 to C16, the second one (topped residue) comprising both hydrocarbons (saturates + aromatics) and polar compounds (resins + asphaltenes). Chemical composition and elemental analysis of the initial samples are reported in tables 1 and 2.

EXPERIMENTAL SIMULATION

The experiments were carried out in sealed gold tubes under pressure; pyrolysis conditions are listed in table 3.

Pyrolysis products were analyzed according to the following procedure (11):

- non hydrocarbon gases:
 - * quantification of individual species such as H₂O, CO₂ and H₂S,
 - * atomic balance for carbon, hydrogen, oxygen and sulfur.
- C1-C5 fraction:
 - * identification and quantification of all hydrocarbons,
 - * carbon and hydrogen balances.
- C6-C13 fraction:

- * separation of saturates plus unsaturates and aromatics,
- * quantification of all saturates,
- * quantification and identification of nearly all aromatics,
- * carbon and hydrogen balances.
- C14+ extract:
 - * separation into saturates, aromatics and NSO compounds and quantification,
 - * elemental analysis of total C14+ fraction
- insoluble residue:
 - * quantification and elemental analysis.

Consequently, atomic balances are done on the total pyrolysis products recovered in each experiment in order to be compared to the elemental analysis of the initial sample. This allows a check of the experimental data independent of the mass balance. Table 4 presents an example of a set of experimental data obtained at 300°C for the Type II kerogen.

Kinetic model for kerogen and oil cracking

Cracking reactions can be described by a set of first order reactions involving the transformation of the initial reactant into new compounds or new chemical classes of compounds, some of them being stable and others unstable in the limits of the experimental domain considered.

A first order reaction obeys the Arrhenius law: $dx/dt = -kx$ where x is the reactant concentration and k , the first order rate constant, is equal to $Ae^{-E/RT}$. The preexponential factor A and the activation energy E are the parameters to be determined by experimental simulation and they are characteristic of each cracking reaction. From our 245 experiments, a general kinetic scheme can be elaborated. It comprises six stable classes, H₂O, CO₂, H₂S, C₁, ARO.S (C₆-C₁₃ stable aromatics such as benzene, toluene, xylenes and naphthalene) and coke and 7 unstable classes, C₂, C₃-C₅, C₆-C₁₃ SAT., C₈-C₁₃ ARO., C₁₄+ SAT., ARO.U (unstable C₁₄+ aromatics such as alkyl and/or naphtheno aromatics, resins and asphaltenes), condensed C₁₄+ aromatics (ARO.C) and residual kerogen (RK). In this scheme, 9 cracking reactions are involved:

1. Kerogen \rightarrow H₂O + CO₂ + H₂S + C₁₄+SAT + ARO.U + RK
2. ARO.U \rightarrow H₂O + CO₂ + H₂S + C₁₄+SAT + C₆-C₁₃ SAT + ARO.C + coke
3. ARO.C \rightarrow C₁ + C₃-C₅ + coke
4. C₁₄+SAT \rightarrow C₃-C₅ + C₆-C₁₃ SAT + C₈-C₁₃ ARO
5. C₆-C₁₃ SAT \rightarrow C₁ + C₂ + C₃-C₅ + C₈-C₁₃ ARO + ARO.C
6. C₈-C₁₃ ARO \rightarrow C₁ + ARO.S + ARO.C
7. C₃-C₅ \rightarrow C₁ + C₂ + C₆-C₁₃ SAT + C₈-C₁₃ ARO
8. C₂ \rightarrow C₁ + C₃-C₅ + C₆-C₁₃ SAT
9. RK \rightarrow C₁ + coke

In each reaction, stoichiometric coefficients multiply each compound or class of compounds formed. In order to reduce the number of free parameters to be experimentally determined, the preexponential factor A is assumed to be the same for all cracking reactions. Then, from these experiments, kinetic parameters such as activation energies and stoichiometric coefficients were calculated, through

optimization successively on each kerogen, each topped oil and each distillate, then on each total oil and finally on the two total oils. Consequently, we have a unified kinetic model for oil cracking (reactions 2 to 8), provided the proportions of chemical classes as defined above are known in the initial oil. For kerogen cracking (reactions 1 and 9), due to the complexity of the initial chemical composition of kerogen, a specific kinetic model is currently proposed for each sample.

CHEMICAL MODELLING

Various quantitative analytical techniques allow us to define a macromolecular structure of kerogen or asphaltenes more or less precisely. These techniques can be divided into 2 classes (Table 5). One includes atomic analyses such as elemental analysis, spectroscopic techniques and the quantitative determination of some functional groups. The other involves quantitative analysis of molecular moieties obtained by degradation reactions such as pyrolysis (12, 13, 14), chemical attack (15, 16) or natural thermal cracking during burial of sediments (17). After fractionation, these molecular moieties can be identified and quantified by chromatography or mass spectrometry. Results provide molecular level information because the inference is that the small molecules are component fragments of the larger macromolecule. As these analytical data are not sufficient to allow a detailed representation of a macromolecular structure, some assumptions, have to be made (Table 6). In order to combine all these informations and to elaborate a chemical model, a new chemical representation of molecules labelled "molecular signature" is proposed: each molecule is defined by a series of 21 coordinate numbers which characterize the geometric configuration of atoms. It can be applied either to molecular moieties or to the macromolecule. Moreover, it allows to calculate parameters not available by analytical techniques. Then a structure is built from the analyses and assumptions defined above, using the software XmolTM (10). A first step is to construct in a 3D space the molecular moieties, including biomarkers, analyzed as described above: this is done by an editor of molecules which stores these data into a library. Then, starting from the set of equations describing the analytical results and the assumptions, a prediction program selects quantitatively the required cyclic or aliphatic groups from the library and calculates a list of intergroup bonds. Finally, a third program constructs in a 3D space one macromolecule isomer calculated by the prediction program. Although each run of the third program will give one different 3D isomer of the macromolecule, the prediction program has an unique solution for one set of analytical data plus assumptions. It thus allows to characterize the macromolecule by the list of its molecular groups or chemical bonds, whatever the arrangement of molecular groups is.

Among the advantages of this software it allows:

- to list all parameters to be known in order to describe the chemical structure of a given macromolecule,
- to compare the number of assumptions versus analytical data, thus testing the accuracy of the chemical structure,
- to stress some discrepancies among the set of analytical data,
- to take into account, at any time new analytical data which may eliminate assumptions,

- to build self consistent chemical structures which fit all analytical data and to calculate easily the number of each atom or bond.

DISCUSSION

When both kinetic scheme of kerogen cracking and corresponding chemical modelling are achieved, the last problem is to link the two fields of research. The aims of this remaining work are to check, for reference samples, the validity of the kinetic scheme by chemical constraints and then to help to predict thermal cracking of an unknown sample according to its chemical structure, without starting again a complete experimental study. Xmol allows us to describe kerogen or related compounds as a set of chemical bonds or molecular groups, for instance:

- a - number of methyl groups,
- b - number of ethyl groups,
- c - number of aliphatic chains from C3 to C5,
- d - number of aliphatic chains from C6 to C13,
- e - number of aliphatic chains C14+,
- f - number of functional groups such as carbonyl, carboxyl, phenols, alcohols methoxy groups and other ethers,
- g - distribution and amount of naphthenic rings,
- h - distribution and amount of naphthenoaromatic rings,
- i - distribution and amount of aromatic rings.

Each of these molecular groups can be considered as individual and independent reactant during kerogen cracking. Thus, when a given molecular group is considered in the general kinetic scheme described above, knowing its initial proportion in the kerogen structure is enough to predict either its contribution among pyrolysis products derived from kerogen cracking or the proportion of pyrolysis products when it is degraded. Moreover, as the main difference between kerogen types relies on their relative amounts of the same molecular groups, an unified kinetic model for cracking of kerogen could be established. It means that Xmol allows first to choose chemical classes to be taken into account in the kinetic scheme, secondly to know the chemical composition of the C14+ fraction defined in reaction 1 and finally to constrain stoichiometric coefficients of reactions from 1 to 9. For instance:

- total aliphatic carbon content included in methane, ethane, C3-C5 compounds, C6-C13 saturates and C14+ saturates must not exceed the aliphatic carbon content of the initial sample,
- oxygen content included in CO₂, H₂O and coke must not exceed the oxygen content in the initial sample,
- oxygen content included in CO₂ must not exceed the oxygen content included in both carbonyl and carboxyl functional groups,

CONCLUSION

We have checked the feasibility of this new approach for relating thermal reactivity and chemical structure of kerogen only from a qualitative point of view. In the future, we have to confirm this feasibility with quantitative data. Moreover, we need to improve our knowledge of the chemical structure of kerogen, especially on the quantitative determination of functional groups, in order to relate a given functional

group to the yield of non hydrocarbon species released during pyrolysis of kerogen (reactions 1 and 2). Finally, specific and more precise additional analyses can be performed on asphaltenes, such as liquid ^{13}C NMR and some chemical degradation techniques, which could better constraint structural parameters and thus kinetic scheme. Nevertheless, use of Xmol must be considered at its current stage of development mainly as an useful guide for writing kinetic equations but not as a predictive tool i.e. as a substitute of experimental work. The very first use of this software is to give a chemical model of an unknown sample which, up to now, has been considered as a "black box". Even if it is only a model which will certainly be modified in the future according to new analytical data, it allows to set up appropriate experimental work for kinetic studies as well for temperature and time conditions as for analytical procedure for identification and quantification of pyrolysis products. A direct application of that work extended to complex products such as resins or asphaltenes could be in refinery processes, for thermal treatment of heavy ends of petroleum. This work allows also to link two fields of research, structure of kerogens (and related compounds) and kinetics, which are generally studied by separate research teams.

REFERENCES

1. Durand B., Kerogen, Editions Technip, Paris, 1980.
2. Ungerer P., Advances in Organic Geochemistry 1989 (Edited by B. Durand and F. Behar), Org. Geochem., Vol 16, Nos 1-3, pp 1-25, (1990).
3. Tissot B., Pelet R. and Ungerer P., AAPG Bull. 71, 12, 1445-1466, (1987).
4. Espitalié J., Ungerer P., Irwin I. and Marquis F., Org. Geochem., 13, 4-6, 893-900, (1988).
5. Burnham A. K. and Braun R. L., In situ, 9 (1), 1-23, (1985).
6. Lewan M. D., Philosophical Transactions of the Royal Society of London, series A, 315, pp. 123-134, (1985).
7. Behar F., Ungerer P., Kressmann S. and Rudkiewicz J. L., Rev. Inst. Fr. du Pétrole, in press, (1991).
8. Burnham A. K. and Braun R. L., Advances in Organic Geochemistry 1989 (Edited by B. Durand and F. Behar), Org. Geochem., Vol 16, Nos 1-3, pp. 27-39, (1990).
9. Kressmann S., unpublished data. (1990).
10. Faulon J. L., Vandenbroucke M., J. M. Drappier, F. Behar and Romero M., Advances in Organic Geochemistry 1989 (Edited by B. Durand and F. Behar), Org. Geochem., Vol 16, Nos 4-6, pp. 981-993, (1990).
11. Behar F., Leblond C. and Saint-Paul C., Rev. Inst. Fr. du Pétrole, Vol 44, 3, 387-411, (1989).
12. Behar F. and Pelet R., J. Anal. Appl. Pyr., 8, 173-187, (1985).
13. Nip M., Tegelaar E. W., de Leeuw J. W. and Schenck P. A., Advances in Organic Geochemistry 1985 (Edited by Leythaeuser D. and Rullkötter J.), Org. Geochem. 10, pp. 769-778, (1987).
14. Hatcher P. G., Wilson M. A., Vassallo A. M. and Lerch H. E., Int. J. Coal Geol., 13, 99-126, 1989.
15. Micke B. and Michaelis W., Advances in Organic Geochemistry 1985 (Edited by Leythaeuser D. and Rullkötter J.), Org. Geochem. 10, pp. 847-858, (1987).
16. Chappe B., Michaelis W. and Albrecht P., Advances in Organic Geochemistry 1979 (Edited by Douglas A. G. and Maxwell J. R.), Pergamon Press, Oxford, (1980).
17. Tissot B. P. and Welte D. H., Petroleum Formation and Occurrence, Springer, Berlin, (1978).

Table 1: Chemical composition (wt%) of Boscan 300+, Pematang 340+ and corresponding distillates.

Sample	C6-C13 SAT.	C6-C13 ARO.	C14+ SAT.	C14+ ARO.	RES.	ASP.	H	C	Distillate
Boscan 300+	0	0	13	37	33	17	10,1	82,4	
Boscan 300-	44	20	20	17	0	0	12,9	87,1	10
Pematang 340+	0	0	59	17	23	1	1,8	86,7	
Pematang 340-	57	7	30	6	0	0	14,3	85,7	37

Table 2: Elemental analysis of the two reference kerogens (wt%)

Sample	C	H	N	O	S org.	Pyrite
Type II	55,34	5,85	1,77	10,7	3,46	22,9
Type III	72,86	5,27	1,86	15,9	1,06	3,08

Table 3: Pyrolysis conditions for experimental simulation of kerogen and oil cracking

Sample	Temperature (°C)	Time (h)	Number of experiments
Type II kerogen	260-500	0,5-1900	70
Type III kerogen	250-500	0,5-1900	50
2 oils	350-500	0,5-1000	60
2 distillates	380-500	0,5-1000	65

Table 4: Mass balances (wt%) obtained for Type II kerogen at 300°C for various heating times

Time (h)	CO ₂	H ₂ O	H ₂ S	C1	C2-C5	C6-C13 SAT.	C6-C13 ARO.	C14+ extract	Residue
1	2,0	1,7	0,4	0,0	0,2	0,1	0,0	8,5	86,9
9	3,4	2,4	0,7	0,4	0,3	0,3	0,1	17,3	75,1
24	4,0	2,8	0,8	0,5	0,4	0,6	0,2	24,2	66,0
240	4,6	4,2	1,9	0,7	3,0	2,7	1,5	31,1	50,0
648	5,1	4,9	2,3	1,2	3,5	3,7	1,6	26,7	51,0
1296	6,0	4,9	2,5	1,5	4,0	3,9	1,7	26,4	49,0

Table 5 : Analytical data needed for kerogen modelling

ANALYTICAL TECHNIQUE	RESULTS
ATOMIC INFORMATION	
Elemental analysis	<div><div></div><div>Number of atoms (C.H.O.N.S.) Amount of Csp² bonded to : - 3 CARBONS - 2 CARBONS and 1 HYDROGEN - 1 OXYGEN or NITROGEN by a single bond - 1 OXYGEN by a double bond Amount of Csp³ bonded to : - Only CARBON and HYDROGEN - 1 OXYGEN by a single bond - 2 OXYGENS by single bonds Distribution of functional groups Density</div></div>
I.R. Spectroscopy + ¹³ C NMR	
Functional-group analysis Pycnometer	
MOLECULAR INFORMATION	
Pyrolysis + Gas chromatography + Mass spectrometry	<div><div></div><div>Histogram of CARBON NUMBERS in ALIPHATIC CHAINS Histogram of NUMBER of RINGS in CYCLOALKANES Histogram of NUMBER of RINGS in AROMATICS and NAPHTHENOAROMATICS</div></div>
Csp ² is a carbon atom with sp ² hybridization (i.e. aromatic or double bonded). Csp ³ a carbon atom with sp ³ hybridization (i.e. naphthenic or aliphatic).	

Table 6 : Hypotheses done for kerogen modelling

Only the elements C, H, O, N, S.
 List of molecular groups included in a library
 List of possible intergroup bonds (only covalent bonds)
 List of possible functional groups and heteroatoms
 Elimination of improbable configurations (i.e. a carbon linked to 3 or 4 oxygens)
 Number of carbon atoms in the model
 Assumptions which supplement analyses (i.e. : percentage of ether linked to 2 aromatic carbons or 2 aliphatic carbons or 1 aromatic and 1 aliphatic carbon)

BOND DISSOCIATION ENERGY CALCULATIONS FOR COAL FRAGMENTS AND MODEL COMPOUNDS

Harriet F. Ades, Audrey L. Companion, and K.R. Subbaswamy
Departments of Physics and Chemistry
University of Kentucky
Lexington, KY 40506-0055

Keywords: Coal liquefaction, quantum chemical calculations, catalysis modeling.

Abstract

Anderson's modified version¹ of the extended Hückel molecular orbital method and the MNDO and AM1 methods of Dewar have been used to study bond cleavage in molecular fragments of interest to coal liquefaction. Geometric conformations, molecular orbital coefficients for the HOMO's and LUMO's, bond dissociation energies, and heats of reaction have been computed and compared for the three methods. Qualitative agreement with experiments for bond cleavage is observed for the three methods for the neutral molecule. However, the modified Hückel method appears to best describe bond cleavage in the presence of an electron-accepting catalyst. Heats of reaction are also calculated for reaction conditions appropriate to the presence of a hydrogen donor.

Introduction

Given the complexity of coal at the molecular level, it is not clear at the outset that useful quantum chemical computations of relevance to coal chemistry can be carried out. However, there are two significant developments that are paving the way for quantum chemical calculations to play a useful role in this field. One is the steady escalation in the power of computers. The other is the synthesis of model compounds that mimic, in a controlled way, aspects of the molecular structure of coal. Careful, quantitative experimental studies on reaction pathways and catalytic action in reactions involving model compounds promise to offer new insights into coal chemistry and the possibility of developing more economical processes for direct liquefaction.

For any modeling of coal to be significant, it must first be shown that the method employed in the study gives meaningful results for model compounds for which experimental results are available. We have begun by performing quantum chemical calculations on 4-(1-naphthylmethyl)biphenyl (referred to hereafter as Model Compound I), studied recently by Farcasiu and Smith.^{2,3} In Figure 1 the skeletal structure of Model Compound I is shown. In their experiments Farcasiu and Smith demonstrated the bond breaking selectivity of a novel catalyst, carbon black (BP 2000), and measured kinetic reaction rates and bond activation energies for cleavage of the methylene and ethylene linkages of the compound. We have recently used^{4,5} several semi-empirical quantum chemical methods to calculate bond dissociation energies of model compounds and coal fragments. In this paper we describe some further calculations that are designed to elucidate the bond-selective catalytic action in the hydrogenation reaction of 4-(1-naphthylmethyl)biphenyl studied by Farcasiu and Smith.^{2,3}

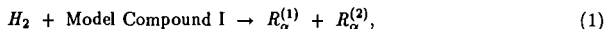
In the earlier papers^{4,5} we used Anderson's modified version of the extended Hückel molecular orbital method¹ and the MNDO and AM1 methods of Dewar, *et al.*^{6,7} to study bond cleavage in

neutral and positively charged Model Compound I. The interest in the positively charged radical ion formed from Model Compound I by removal of an electron comes from the suggestion of Farcasiu and Smith^{2,3} that the BP 2000 catalyst acts as an electron acceptor and removes an electron from the naphthyl portion of model compound I.

Geometric conformations, molecular orbital coefficients for the HOMO's and LUMO's, and bond dissociation energies were computed and compared for the three methods. Qualitative agreement with experiment for bond cleavage was observed for the three methods for the neutral molecule. Our earlier calculations suggest that the ASED-MO method appears to best describe the bond cleavage in the presence of an electron-accepting catalyst. This can be seen from the results shown in Table 1, where the product distributions with and without the catalyst (i.e., for the neutral molecule and the positive radical ion, respectively) calculated by the ASED-MO method are compared with the thermolysis results. The bond labels referred to in the Table are shown in Figure 1. The theoretical relative product distributions were calculated from the computed bond dissociation energies (shown in columns 2 and 5) using the Boltzmann distribution at the experimental temperature. The qualitative agreement between theory and experiment with regard to the bond-selectivity of the catalytic reaction is evident from the Table.

Calculation of Energies of Reaction

In our earlier papers the reactions in the presence of a hydrogen donor, which are more directly relevant to the study of coal liquefaction, were not studied. In this paper we have calculated the energy differences for the five reactions



where $\alpha = a, b, c, d, e$ denotes the bond that is cleaved in the reaction (as labeled in Figure 1), and in each instance, $R^{(1)}$ denotes the product molecule containing the naphthyl portion of the starting Model Compound I and $R^{(2)}$ the product molecule containing the remainder of Model Compound I. This is a rather simplistic model of the reaction in the presence of the hydrogen donor; clearly, the energy of reaction for hydrogen extraction from the donor (e.g., 9,10-dihydrophenanthrene) will be involved. However, our interest is in the relative product stabilities for the different bond cleavages, and the hydrogen extraction contribution should be essentially the same in all the cases. We present results for ASED-MO, MNDO, and AM1 methods. It should be noted that only the relative energies of reaction for the five paths indicated above within any given method are significant. The absolute numbers calculated by the different methods depend on the calculated dissociation energy for the hydrogen molecule. For example, the dissociation energy for the hydrogen molecule is overestimated by about 5 eV by the ASED-MO method, and by about 1 eV by the AM1 method.

In Table 2 we show the energies of reaction for the hydrogenation reactions of the neutral and charged Model Compound I calculated by the three methods. As explained above, only the relative magnitudes within each method are meaningful. For reactions involving the positive radical ion, the positive charge is kept with the product species containing the naphthyl fragment; the justification for this has been given in our earlier papers. The main conclusion from Table 2 is that the energies of reaction for the five different paths are similar; the product stabilities relative to the reactants are not greatly different, and further there is no correlation between product stability and the observed product distributions. This is true for reactions involving the neutral molecule as well as the positive radical ion.

Discussion and Conclusions

From these calculations we conclude that the driving force behind the bond-selectivity found in the reaction is not the relative thermodynamic stabilities of the products formed. Other possible factors for the bond selectivity are the differences in the activation energies for the different bond cleavages, and/or the charge distribution in the radicals formed after bond cleavage. We will consider first whether the experimentally found product distribution might be accounted for by the differences in the hydrogen affinity of the radicals formed by the bond cleavage. To test the importance of this factor, we have compared the charge localized on the terminal carbon atoms of the cleaved bond for the neutral and the charged Model Compound I in the different methods. We find no correlation between the charge build-up in the radicals and the observed product distributions.

Since the entropy changes in all the reactions are expected to be small, the bond dissociation energies, which are directly calculated by the theoretical methods, should be an upper bound to the activation energies and appears to be the most important factor in determining the product distributions. The ASED-MO method predicts the difference between the neutral molecule and the positive radical ion in qualitative agreement with experiment. The fact that this simple method succeeds where the more sophisticated semi-empirical methods fail is surprising. Of course, the MNDO and AM1 methods have not really been parameterized for charged species, and this may be the reason for their apparent failure. We are presently carrying out more calculations both to further elucidate the catalytic action, and to test the methods for other model compounds.

Acknowledgments

This research was supported in part by the USDOE through contract DE-FC22-90PC90029. We are grateful to Dr. Malvina Farcasiu for providing us with the experimental data on Model Compound I prior to publication.

References

1. Anderson, A.B. *J. Chem. Phys.*, **1974**, *60*, 2477.
2. Farcasiu, M.; Smith, C. *Prepr., Div. Fuel Chem., Am. Chem. Soc.* **1990**, *35*, 404.
3. Farcasiu, M.; Smith, C. *Energy Fuels* (in press)
4. Ades, H.F.; Companion, A.L.; Subbaswamy, K.R. *J. Phys. Chem.* (in press).
5. Ades, H.F.; Companion, A.L.; Subbaswamy, K.R. (to be published).
6. Dewar, M.J.S.; Thiel, W. *J. Am. Chem. Soc.* **1977**, *99*, 4899.
7. Dewar, M.J.S.; Zoebisch, E.G.; Healy, E.F.; Stewart, J.J.P. *J. Am. Chem. Soc.*, **1985**, *107*, 3902.

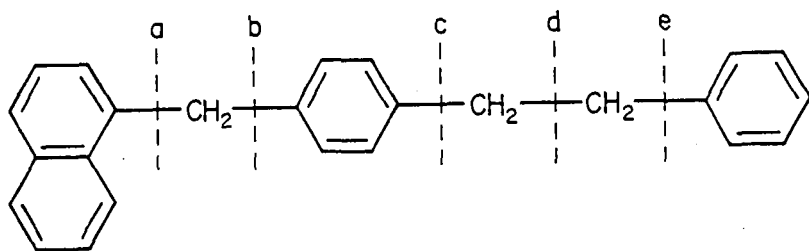


Figure 1: The skeletal structure of 4-(1-naphthylmethyl)bibenzyl. The methylene and ethylene linkages, whose cleavage is of interest here are labeled for use in the text.

Bond	Neutral			Charged (+1)		
	BDE(eV)	Product %		BDE(eV)	Product %	
	ASED	ASED	Expt. ^a	ASED	ASED	Expt. ^a
a	4.09	0.4	17	2.80	94	51
b	3.89	11	3	3.08	0.7	7
c	4.23	0.0	16	3.01	2	8
d	3.77	88	64	3.00	3	34
e	4.18	0.1	-	3.40	0.0	-

^aFrom Farcasiu and Smith (Ref. 2)

Table 1: Bond dissociation energies (BDE) and product distributions for the thermolysis of Model Compound I. The results for the positively charged radical ion are appropriate to the presence of BP 2000 catalyst, as described in the text. From Ades, *et al.*, Ref. 5.

Bond	ASED-MO		MNDO		AM1	
	Neutral	Charged	Neutral	Charged	Neutral	Charged
a	0.90	0.96	-0.60	-0.54	-0.12	0.00
b	0.93	0.98	-0.43	-0.44	-0.02	-0.09
c	0.93	0.93	-0.37	-0.43	0.05	-0.02
d	1.07	1.07	-0.50	-0.55	-0.03	-0.10
e	0.93	0.93	-0.37	-0.42	0.05	-0.03

Table 2: The calculated energies of reaction (in eV) for the neutral and charged (+1) Model Compound I using three semi-empirical methods. As explained in the text the numbers are only meaningful for the comparison of the thermodynamic stability of the products relative to the reactants within a particular method.

AN INVESTIGATION INTO THE REACTIVITY OF ISOTETRALIN

M. W. Bedell, C. W. Curtis
Department of Chemical Engineering
Auburn University, Auburn, AL 36849

Keywords: molecular orbital, hydrogen transfer, isotetralin

ABSTRACT

Molecular orbital calculations were used to explore proposed reaction mechanisms of isotetralin (ISO) and tetralin (TET). Heats of formation and electronic data were determined for ground states and intermediate species. Since the reaction mechanisms was not known a priori, calculations were performed for anionic, cation and free radical dehydrogenation mechanisms. The electron density in the frontier molecular orbitals was used to assess the relative reactivity of sites within ground state and radical species. Model reactivity studies examining the thermal and catalytic reactivity of ISO and TET were performed. ISO was much more reactive than its isomeric analogue TET. Possible reaction pathways are proposed based upon the product slate obtained in the model compound reactivity experiments that were performed at 225, 380 and 425°C with ISO, TET, 1,4-dihydronaphthalene and 1,2-dihydronaphthalene. The results from the experimental study were evaluated in light of the results obtained from the molecular orbital calculations.

INTRODUCTION

The cyclic olefin, isotetralin, (1,4,5,8-tetrahydronaphthalene) is a highly effective donor for coal conversion at liquefaction temperatures. In previous experimental work, isotetralin converted more coal to THF solubles under thermal liquefaction conditions in both nitrogen and hydrogen than did tetralin (1,2). The results of experimentally evaluated reactivities and reaction pathways under a variety of conditions have recently been reported by Bedell and Curtis (2). The observed high reactivity and hydrogen donability of isotetralin warrants further investigation to understand its mechanism of hydrogen donation and a subsequent investigation of how that information can be applied to processing.

The focus of this report is to examine the dehydrogenation mechanism of ISO and TET using molecular orbital calculations and to compare the calculated results with those obtained experimentally. To achieve this goal, calculations were performed using a semi-empirical method of modified neglect of diatomic overlap (MNDO), developed by Dewar and Thiel (3). The second part of the investigation determined the most likely site for hydrogen donation from each donor molecule, by using frontier molecular orbital electron densities (4).

EXPERIMENTAL RESULTS

Isotetralin Reactivity. Isotetralin (ISO) showed much greater reactivity than did tetralin when reacted at temperatures of 225 and 380°C under both nitrogen and hydrogen atmospheres in stainless steel tubing bomb reactors at different reaction times. ISO converted rapidly and formed the reaction products of 1,2-dihydronaphthalene (1,2-DHN) 1,4-dihydronaphthalene (1,4-DHN), tetralin (TET) and naphthalene (NAP). The same products were formed regardless of the atmosphere, but different amounts were present as shown in Table 1. After two minutes of reaction at 380°C in either nitrogen on hydrogen, nearly 50% of the ISO converted producing 1,4-DHN as

the primary product. Longer reaction times in either nitrogen or hydrogen resulted in all of the ISO being converted. Conversely, TET showed little reactivity at 380 or 425°C. Even after 30 minutes of reaction in either atmosphere at 380°C, less than 5% conversion of TET was obtained. Reactions of TET for 15 minutes at 425°C resulted in 20% conversion in nitrogen and ~ 12% in hydrogen. The products formed in each case were 1,2-DHN, 1,4-DHN and NAP.

Reaction Pathway for Isotetralin. A proposed thermal dehydrogenation reaction pathway based on the products obtained from reactions performed with ISO at 225 and 380°C in nitrogen and hydrogen atmospheres is presented in Figure 1. In addition, reactions were performed using reaction products from ISO as the reactants to further elucidate the reaction pathway. The product distributions from reactions involving 1,2-DHN and 1,4-DHN are presented in Table 2. Short time (2 minute) reactions of 1,4-DHN in either nitrogen or hydrogen at 225 or 380°C resulted in ~ 25% or less of the 1,4-DHN being converted to the products, NAP and 1,2-DHN. No TET was formed. The reaction products observed from a 30 minute reaction of 1,4-DHN at 380°C were TET, 1,2-DHN, and NAP in hydrogen and NAP and TET in nitrogen; 1,4-DHN readily isomerized to 1,2-DHN. More NAP was produced in nitrogen than in hydrogen and substantially more TET was produced from 1,4-DHN in hydrogen after 30 minutes of reaction than in nitrogen.

The reaction of 1,2-DHN was also examined under a variety of conditions as presented in Table 2. Thermal reactions were performed at 425°C for 15 minutes while catalytic reactions using two different hydrogenation catalysts were performed at 225 and 380°C for short 2-minute reactions. Under catalytic conditions in hydrogen, 1,2-DHN preferentially produced TET as a product while under thermal conditions NAP was the preferred product. Some isomerization of 1,2-DHN to 1,4-DHN did occur indicating that the isomerization pathway to TET may also be available.

The thermal reactions of TET shown in Table 1 are inconclusive of a preferential pathway for TET reaction to 1,2-DHN. This pathway is obscured because of the observed isomerization of 1,2-DHN to 1,4-DHN. However, the reaction of 1,2-DHN particularly under catalytic conditions indicated that TET was the preferred product. On the basis of microscopic reversibility, it would be appropriate to suggest that TET may preferentially form 1,2-DHN in the dehydrogenation reaction.

The thermal dehydrogenation pathway of ISO proposed then is (1) the isomerization of ISO to form TET as indicated by the formation of TET in the 380°C reactions in both nitrogen and hydrogen and in (2) the dehydrogenation of ISO to form 1,2-DHN or 1,4-DHN as indicated by both the short time and longer reaction products in both atmospheres. 1,4-DHN appeared to be the favored product except at 60 minute reaction time in hydrogen. The isomerization step from ISO to TET in the pathway resulted in further dehydrogenation of TET to 1,2-DHN or 1,4-DHN. The DHN's then dehydrogenated to form NAP as indicated by the dehydrogenation of 1,4-DHN to NAP at all reaction conditions.

MOLECULAR ORBITAL CALCULATIONS

It has been reported in the literature on polyaromatic hydrocarbons that the electron density in the frontier molecular orbitals of the carbon or heteroatoms can be used, with some degree of success as an indicator of reactivity (4, 6-8). Sato et al. (6) found good agreement between the experimentally determined reactivity ranking of 1-methylnaphthalene, tetralin, decalin, and 9,10-dihydroanthracene, with that predicted by the electron density in the frontier molecular orbitals. Obara et al. (7) experimentally found that for a series of compounds, the ease of hydrogenation was acenaphthylene > anthracene > phenanthrene, and reported that "this order is in good agreement

with that in the terms of frontier electron density at a given position of the compounds" (7). Sukano et al. (8) found that the conversion of the donor increased with increasing electron density of the carbon and oxygen atoms of the carbonyl groups in the hydrogen acceptors.

Molecular orbital (MO) calculations were performed to elucidate the reasons for the greater reactivity observed for ISO in comparison to TET and to more fully investigate the dehydrogenation pathway proposed from experimental results. These MO calculations were performed using SYBYL (licensed from Tripos Associates, Inc.), which is an integrated molecular modeling package with graphics and interfaces to various computational methods. The desired structures were input using the graphics capabilities of SYBYL, with standard bond lengths and angles. These structures were next optimized using the Tripos 5.2 force-field (5) and conjugate gradient minimization. The resulting optimized structures were used as input to AMPAC (QCPE 506) using the MNDO Hamiltonian, with complete geometry optimization. MO calculations were performed on a VAX 5320 computer, while the force-field calculations were done on a MicroVaxII and Sparcstation 1+ workstation.

Since the actual dehydrogenation mechanism was not known a priori, three separate routes were investigated; they were cationic, anionic, and two proposed free radical pathways. MNDO calculations were performed on the ground state reactants (ISO or TET), the single radical or charged intermediate, the bi-radical or dual charge species, and finally the ground state product. The molecular orbital procedures used are capable of determining energetic, electronic and structural data. For the current investigation, the thermodynamic stability of each step was assessed through heats of formation.

Calculations on the open shell species (free radicals) were performed using the half electron approximation, in which the unpaired electron is represented by two "half electrons" with opposite spin. The repulsive energy introduced by this convention is subtracted from the final energy value. The energies calculated in this way can be directly compared to those for closed shell species.

Frontier orbital density was determined as the electron density in the highest occupied molecular orbital (HOMO) for closed shell species, and the singly occupied molecular orbital (SOMO) for radicals. These values are determined as the sum of squares of the atomic orbital coefficients for a given atom. These values are multiplied by one and two for open and closed shell structures, respectively.

DEHYDROGENATION MECHANISM

Based on the experimental results that have been previously discussed and presented in Figure 1, MNDO calculations were performed for the transitions between reactants and products from ISO to 1,4-DHN and TET to 1,4-DHN, and the other dehydrogenation paths illustrated. Initial work focused on the former pathways, since they appear to be preferred to the 1,2-DHN pathway. As indicated, cationic, anionic, and radical routes were examined. The calculated heats of formation for the proposed compounds in each step are shown in Figures 2 and 3.

Frontier Orbital Electron Density Calculations. Based on these results, the distribution of electron densities was examined for each step in the free radical pathway. As indicated in the cited literature, it has been proposed that the higher the frontier electron density $F_i(R)$, the more reactive the site; i.e., the hydrogen most likely to be removed will have the highest electron density. The results of these frontier orbital electron density calculations for ISO and TET are presented in Figures 4 a-d and 5 a-e, respectively.

Figure 4-a shows the frontier electron density for the donable hydrogen in ground state ISO. As can be seen, the hydrogen on carbons 1,4,5, and 8 are approximately equivalent, and the loss of a hydrogen is not expected to be preferential to any one of the four positions. For illustrative purposes, if the hydrogen is lost from carbon 8, the radical species shown in Figure 4-b will be formed. Evaluating the resulting electron densities, the second hydrogen will be lost from carbon 5, which has the highest electron density. The resulting bi-radical species formed is shown in Figure 4-c. Once this species is formed, the double bond will isomerize to either the 7-8 or 5-6 positions, both of which are equivalent. The new bi-radical species formed is shown in Figure 4-d, and once the radicals are on adjacent carbon centers, a double bond will form to produce 1,4-DHN (Figure 4-e). These frontier molecular orbital electron density calculations predict that ISO will dehydrogenate preferentially to 1,4-DHN which is in good agreement with the experimental results.

Figure 5-a shows $Fr(R)$ for the donable hydrogen in ground state TET. The electron densities for the hydrogen atoms at carbons 1 and 4, using the IUPAC numbering system for naphthalene parent compound are greater than those of the hydrogen atoms on carbons 2 and 3. Assuming that the loss of hydrogen occurs at the position with the highest electron density indicates that dehydrogenation occurs at carbon 4. Removal of the hydrogen at carbon 4 level forms the single radical species shown in Figure 5-b. It is predicted that the second hydrogen will be removed from carbon 3, the position with the highest electron density in the single radical species, to form the bi-radical shown in Figure 5-c. Once the bi-radical species is formed, the free electrons will combine to form a double bond, producing 1,2-DHN (Figure 5-d). The frontier orbital electron density calculations predict that TET will preferentially be dehydrogenated to 1,2-DHN, which appears to be what the experimental results previously described suggest. From the calculations for the frontier orbital electron density of ISO and TET, and the comparison with experimental results, $Fr(R)$ appears to be a useful predictive and explanatory tool in the investigation of the dehydrogenation of cyclic olefins and hydroaromatic compounds.

SUMMARY OF THEORETICAL STUDY

The MNDO calculations, coupled with the frontier molecular orbital electron density calculation, are in good agreement with the experimentally determined results in the following points: 1) ISO is readily converted to 1,4-DHN and TET, and only to a small extent to 1,2-DHN. 2) TET is preferentially converted to 1,2-DHN. 3) ISO is more reactive than TET because of its lower energy barrier for 1,4-DHN formation, more possible reaction pathways, and its larger $Fr(R)$ value on the greater number of donable hydrogen. These results illustrate the potential of molecular orbital calculations to be a useful tool in the understanding of fundamental dehydrogenation chemistry of model hydrogen donor compounds.

1. Curtis, C.W.; Guin, J.; Kwon, K.; "Coal Solvolysis in a Series of Model Compound Systems," *Fuel*; 63; 1984.
2. Bedell, M.W.; Curtis, C.W.; "The Chemistry and Reactivity of Cyclic Olefins as Donors in Coal Liquefaction," Submitted to Energy and Fuels; 11/90.
3. Dewar, M.; Thiel, W.; *Am. Chem. Soc.* 1977, 99, 4899.
4. Fukui, K.; Yonezawa, T.; Nagata, C.; *Bull. Chem. Soc. Japan*, 1954, 27, 423.
5. TRIPOS ASSOCIATES, INC., St. Louis, Missouri, 1989.
6. Sato, Y.; Uemasu, I.; Kushigama, S.; *Proceeding 1985 International Conference on Coal Sciences*; Sydney, Aust.
7. Obara, T.; Yokono, T.; Sanada, Y.; *Fuel*, 1983, 62, 813-816.
8. Sukeno, Toshio; Tsutsumi, Kinto; *Oyama Kogyo Koto Senmon Gakko Kenky Kiyo*, Vol. 14, 94-97, 1982.

Table 1. Reactivity of Isocetralin and Tetralin

Donor	Temperature (°C)	Atmosphere	Time (min)	NAP	1,2-DH	1,4-DH	TEF	ISO
ISO	225	H ₂	2	0.0	0.0	2.8(0.3)	0.0	97.2(0.3)
	380	H ₂	2	2.0(0.1)	0.0	48.4(0.5)	1.6(0.1)	46.4(0.3)
	380	H ₂	30	55.1(1.5)	4.0(0.5)	36.7(1.0)	3.6(0.4)	0.0
ISO	225	H ₂	2	0.0	0.0	1.7(0.3)	0.0	98.3(0.3)
	380	H ₂	2	2.2(0.2)	3.1(0.7)	39.1(1.8)	3.3(1.5)	52.3(2.9)
	380	H ₂	15	30.5(0.5)	23.8(4.6)	27.9(12.3)	17.8(6.0)	0.0
	380	H ₂	30	52.6(2.3)	10.0(2.6)	26.8(3.7)	10.6(1.2)	0.0
	380	H ₂	60	61.1(2.1)	11.5(1.7)	1.1(0.3)	26.3(3.5)	0.0
TEF	380	H ₂	30	0.8(0.2)	0.0	0.0	99.3(3.8)	0.0
	425	H ₂	15	1.2(0.02)	12.5(0.6)	6.3(0.4)	80.0(1.2)	0.0
TEF	380	H ₂	30	0.7(0.1)	1.0(0.1)	2.1(0.3)	96.2(2.3)	0.0
	425	H ₂	15	0.0	3.5(0.2)	8.6(0.1)	87.9(0.3)	0.0

Table 2. Reactivity of 1,4-Dihydronaphthalene and 1,2-Dihydronaphthalene

Donor	Temperature (°C)	Atmosphere	Time (min)	Catalyst	NAP	1,2-DH	1,4-DH	TEF	ISO
1,4-DH	225	H ₂	2	none	10.7(1.7)	10.9(0.3)	78.4(1.5)	0.0	0.0
	380	H ₂	2	none	13.1(0.2)	11.3(0.2)	75.4(0.2)	0.0	0.0
	380	H ₂	30	none	60.2(1.7)	0.0	28.5(1.6)	11.3(0.8)	0.0
	225	H ₂	2	none	9.2(0.3)	11.0(0.2)	79.8(0.3)	0.0	0.0
	380	H ₂	2	none	13.0(0.2)	12.8(0.9)	74.2(1.1)	0.0	0.0
	380	H ₂	30	none	44.9(0.3)	11.5(0.3)	1.7(0.5)	41.9(0.6)	0.0
1,2-DH	425	H ₂	15	none	43.6(0.04)	42.4(0.3)	9.1(0.3)	4.7(0.1)	0.0
	425	H ₂	15	none	40.5(0.6)	46.1(0.8)	8.2(0.3)	4.8(0.1)	0.0
	225	H ₂	2	Mo/Al ₂ O ₃	trace	44.7(0.4)	trace	55.3(0.4)	0.0
	325	H ₂	2	NiMo/Al ₂ O ₃	0.0	17.3(6.5)	3.1(0.5)	79.6(6.0)	0.0
	380	H ₂	2	NiMo/Al ₂ O ₃	0.0	0.0	0.0	99.9(4.7)	0.0
	380	H ₂	2	NiMo/Al ₂ O ₃	9.1(4.7)	0.0	0.0	90.9(4.7)	0.0

Reaction Conditions: 425 cps, 1250 psig H₂ or H₂ charge at ambient temperature, 2.0 g charge of 0.5 weight percent deuterium hydrogen in hexadecane.

Abbreviations:

NAP = naphthalene; 1,2-DH = 1,2-dihydronaphthalene; 1,4-DH = 1,4-dihydronaphthalene; TEF = tetralin; ISO = isocetralin.

Figure 1. REACTION PATHWAY FOR ISOTETRALIN.

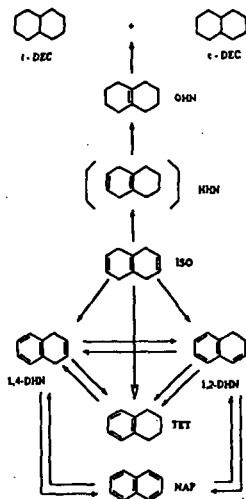


Figure 2. HEAT OF FORMATION DATA FOR THE TRANSITION OF ISO TO 1,4-DHN: THREE MECHANISMS.

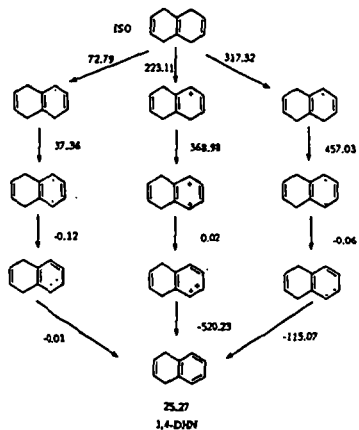


Figure 3. HEAT OF FORMATION DATA FOR THE TRANSITION OF TET TO 1,4-DHN: THREE MECHANISMS.

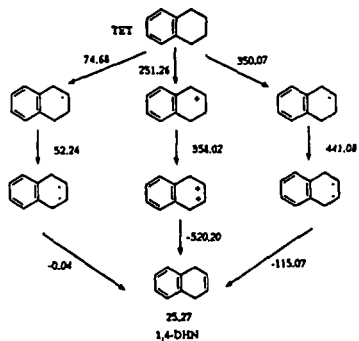


Figure 4. ELECTRON DENSITIES IN THE TRANSITION OF
ISO TO 1,4-DHN .

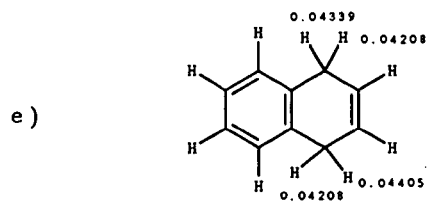
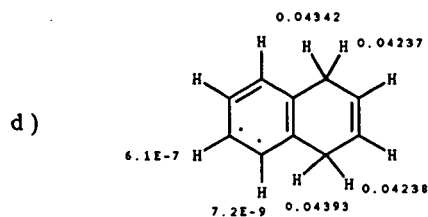
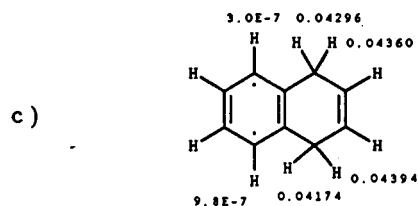
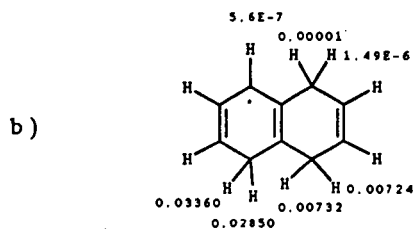
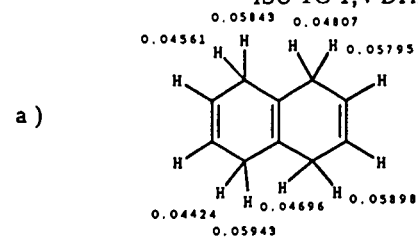


Figure 5. ELECTRON DENSITIES IN THE TRANSITION OF
TET TO 1,2-DHN.

